NEUROSCIENCE

An in vitro neurogenetics platform for precision disease modeling in the mouse

Daniel E. Cortes, Mélanie Escudero, Austin C. Korgan, Arojit Mitra, Alyssa Edwards, Selcan C. Aydin, Steven C. Munger, Kevin Charland, Zhong-Wei Zhang, Kristen M. S. O'Connell, Laura G. Reinholdt, Martin F. Pera*

The power and scope of disease modeling can be markedly enhanced through the incorporation of broad genetic diversity. The introduction of pathogenic mutations into a single inbred mouse strain sometimes fails to mimic human disease. We describe a cross-species precision disease modeling platform that exploits mouse genetic diversity to bridge cell-based modeling with whole organism analysis. We developed a universal protocol that permitted robust and reproducible neural differentiation of genetically diverse human and mouse pluripotent stem cell lines and then carried out a proof-of-concept study of the neurodevelopmental gene *DYRK1A*. Results in vitro reliably predicted the effects of genetic background on *Dyrk1a* loss-of-function phenotypes in vivo. Transcriptomic comparison of responsive and unresponsive strains identified molecular pathways conferring sensitivity or resilience to *Dyrk1a1A* loss and highlighted differential messenger RNA isoform usage as an important determinant of response. This cross-species strategy provides a powerful tool in the functional analysis of candidate disease variants identified through human genetic studies.

INTRODUCTION

There is an increasing awareness of the importance of genetic diversity in cellular disease modeling, both for scientific reasons, and in relation to the issue of equitable access to biomedical innovations arising from in vitro discovery platforms (*1*). The scientific benefits of genetic diversity in disease modeling extend to studies in vivo. Most mouse models for heritable human disorders have been created in one or two commonly used inbred strains. However, genetic background can have profound effects on the phenotype of a particular mouse model. Thus, creating a gene knockout or mutation model on a single genetic background may or may not yield a phenotype relevant to human disease. This impediment to precision disease modeling has long been apparent from studies of mouse knockouts on different genetic backgrounds (*2*, *3*) and can generally be related to the effects of modifier genes (*4*).

To a considerable degree, incorporating greater genetic diversity into disease modeling in the mouse can provide a more reliable reflection of human disease pathogenesis than studies with a few inbred strains. A number of recent reports have shown clearly how the use of genetically diverse strain backgrounds can enhance our ability to model human sensitivity and resilience to disease, as exemplified in studies of Alzheimer's disease, type 2 diabetes, autism, and gastric cancer (*5*–*13*). However, the establishment, maintenance, and use of mouse diversity panels require substantial infrastructure, animal husbandry, and genetics resources, limiting their implementation for many investigators.

In recent years, mouse embryonic stem cell (mESC) lines from genetically diverse mouse strains have become available, and they have been used in vitro to study the genetic basis of the permissiveness of strains for mESC establishment, the regulation of the pluripotent state and early lineage specification, and the stability of genomic imprinting in vitro (*10*–*12*, *14*–*18*). To apply these approaches in disease modeling, it is important that differentiation protocols provide

for similar high yields of relatively pure cell populations across genetically diverse cell lines. Here, we report a paradigm for the application of genetically diverse mESC lines to in vitro disease modeling in the central nervous system (CNS), a precision neurogenetics approach that has the potential to make mouse genetic diversity more accessible to the research community, and to provide for facile selection of appropriate mouse genetic backgrounds for human disease modeling.

Experimental platforms based on human pluripotent stem cells (hPSCs), including two-dimensional (2D) cultures and 3D organoid models of specific brain regions, are playing an increasing role in the study of the development of the CNS and in unraveling the genetics of brain disorders (*19*). However, most neurologic or psychiatric disorders are highly complex, involving the interaction of multiple systems inside and outside of the CNS and behavioral phenotypes that cannot be observed in vitro. We aimed to provide a facile link between human disease models and mouse diversity genetics to enable precision disease modeling. We first established a set of robust universal neural differentiation protocols that enable production of key CNS cells of interest from genetically diverse mouse inbred strains and hPSC. These protocols are applicable across mESC and hPSC representative of wide genetic diversity, encompass multiple stages of neural development, and provide for functional readouts. Using high-content screening (HCS), RNA sequencing (RNA-seq), electrophysiology, axonal regeneration paradigms, and knockout models, we provide a proof-of-concept study in the form of a chemogenomic and genetic analysis of the effects of loss of the neurodevelopmental gene, dual-specificity tyrosine phosphorylation–regulated kinase 1A (*Dyrk1a*), at multiple stages of neurogenesis and axonal repair. *Dyrk1a* was first found in *Drosophila*, and the gene named "minibrain" because mutations in the gene causes size reduction of the optic lobes and central brain hemispheres (*20*). *Dyrk1a* gene dosage affects many stages of neural development. In human, *DYRK1A* is located on chromosome 21, and it has been associated with a range of conditions including Alzheimer's disease, Down syndrome, microcephaly, autism, and intellectual disability

The Jackson Laboratory, Bar Harbor, ME 04660, USA.
*Corresponding author. Email: martin.pera@jax.org

(*21–26*). Patients harboring the same point mutation in the *DYRK1A* gene display different phenotypes ranging from severe autism to relatively minor neurological impairment (*25*), strongly suggesting that the genetic background modifies the penetrance of the mutation, similar to many neurodevelopmental disorders.

Using genetically diverse mESC, we demonstrate the impact of genetic background on the outcome of DYRK1A inhibition or loss across multiple stages of neural development. With this approach, matching in vitro phenotypes in hPSC-based disease models with mESC models exhibiting similar sensitivity to pathogenic mutations enables rapid selection of mouse genetic backgrounds for in vivo modeling studies and will provide a platform for prospective analysis of the power of in vitro mutant phenotyping to predict disease phenotype in vivo, a critical component of functional genomics analysis going forward.

RESULTS

To achieve our objectives in precision disease modeling, we had to develop and validate in vitro methodology for the assessment of the effects of genetic variants on neural development and disease across eight highly genetically diverse mESC representing the founders of the Collaborative Cross [CC founders, A/J (AJ), C57BL/6J (B6), 129S1/SvlmJ (129), NOD/LtJ (NOD), NZOHiLtJ (NZO), CAST/EiJ (CAST), PWD/PhJ (PWD, in place of the closely related PWK/PhJ), and WSB/EiJ (WSB)] and to carry out cross-species comparisons with hPSC. First, we developed universal differentiation protocols that functioned efficiently, and then, we tested the validity of our in vitro platform for its ability to predict how individual genotypes would respond to disease mutations.

Initially, we trialed widely cited differentiation protocols used to generate neurons from mESC (*27–32*) across a genetically diverse stem cell panel. These protocols failed when applied to strains other than 129. Therefore, we developed the protocol shown in fig. S1A. With mESC from the B6 strain, by day 8, abundant neurites and neural rosettes are visible (fig. S1B), and cells were passaged for expansion using epidermal growth factor (EGF) and fibroblast growth factor 2 (FGF2) for 3 days. Decay in pluripotency markers and increase in neural markers were revealed by quantitative polymerase chain reaction (qPCR) (fig. S1C). At the end of this period, cells could be frozen or passaged for further maturation by the withdrawal of mitogens and the addition of growth factors.

After the withdrawal of mitogens, neural progenitor cells (NPCs) exited the cell cycle and started to generate more elongated processes (Fig. 1A). The timing of differentiation was similar across all strains (fig. S2). After 7 days of differentiation, neurons represented around 90% of the overall cell population among all strains studied (Fig. 1, B and C). Among these neurons, glutamatergic cells represented around 75% of the neuronal population (Fig. 1, D and E). Practically, all neurons expressed the forebrain marker FoxG1, and cells expressing all individual six cortical layer markers were observed across all analyzed strains at similar frequencies (Fig. 1, B and E). We also analyzed the electrophysiological activity using whole-cell patch clamp. Evoked action potentials were elicited as well as spontaneous activity, both appearing in cultures of all strains after 2 weeks of differentiation (Fig. 1F) and coinciding with the presence of pre- and postsynaptic proteins (Fig. 1D). Using multielectrode arrays (MEAs), we found spontaneous field potentials (Fig. 1G, left) and network activity in all strains (Fig. 1G, right). We could also produce cortical organoids that displayed spontaneous calcium signaling (Fig. 1, H and I).

Modifications to the protocol, using morphogens to achieve patterning, enabled us to generate motor neurons, GABAergic neurons, and dopaminergic neurons from all strains tested at similar efficiencies (Fig. 2). We reasoned that by adjusting the developmental timing between mouse and human cultures (Fig. 3A), our protocol could be adapted to differentiate neurons from hPSC of diverse genetic backgrounds. We tested 10 genetically diverse hPSC from the iPSC Consortium for Omics Research (iPSCORE) representing equally both sexes and diverse ancestries. Once again, we were able to obtain neural progenitors and cortical neurons, and we found that all cell lines differentiated with similar efficiencies regardless of their genetic background (Fig. 3, B and C); we observed spontaneous synchronous electrical activity in these cultures (Fig. 3D). With appropriate patterning (Fig. 3E), we obtained motor neurons that also showed network activity (Fig. 3, F and G), as well as cortical and midbrain dopaminergic organoids that displayed spontaneous calcium signaling (figs. S3 and S4 and movie S1).

Having developed this differentiation platform, we proceeded to conduct a proof-of-concept study to examining how genetic background affects the effect of DYRK1A inhibition during neuronal development at different stages. *Dyrk1a* also regulates axonal growth and guidance, so we decided to assess an experimental model of axon regrowth as well. In most studies, we used the well-characterized DYRK1A inhibitor ID-8; this inhibitor is highly selective against DYRK1A compared to other kinases. ID-8 median inhibitory concentration values for DYRK1A, GSK3b, and CLK1 are 78, 450, and 4200 nM, respectively, and DYRK2, DYRK3, and DYRK4 are not affected at all (*33–36*).

To ascertain that differences in phenotypes observed in response to DYRK1A inhibition or haploinsufficiency were not merely a consequence of differences in gene coding sequences (and by extension protein structure) or expression levels across the strains, we examined both (fig. S5). Despite some divergence in the gene sequences, notably for CAST and PWD (fig. S5A), the single nucleotide variants (SNV) do not affect the protein sequence, and all variants are synonymous (table S1). Examination of expression quantitative trait loci (eQTL) in mESC (*15*, *37*) revealed a local eQTL in CAST and PWD/K (fig. S5B). Nevertheless, we could not find any protein QTL among all the strains in mESC, and direct measurement of protein levels in mESC revealed that although there is a slight decrease of DYRK1A protein in CAST, NOD, and PWD, these differences were not statistically significant (fig. S5, C to E; and for neural progenitors, for neural progenitors, see the section "DYRK1A inhibition differentially blocks neural progenitor proliferation in a strain-dependent fashion").

Effects of DYRK1A inhibition on mESC maintenance and lineage specification vary across genetically diverse mouse strains

It was previously shown that DYRK1A inhibition by ID-8 in mESC and hPSC helps to maintain the pluripotent state and that either chemical inhibition or knockdown hampers specification from the pluripotent state to the neural lineage in hPSC (*33*, *36*). To study pluripotency maintenance and lineage biases across mESC from different strains to compare with previous work on 129 mESC and hPSC, we cultured the eight mESC lines in media supplemented with four combinations of factors: leukemia inhibitory factor (LIF) + 2i [LIF
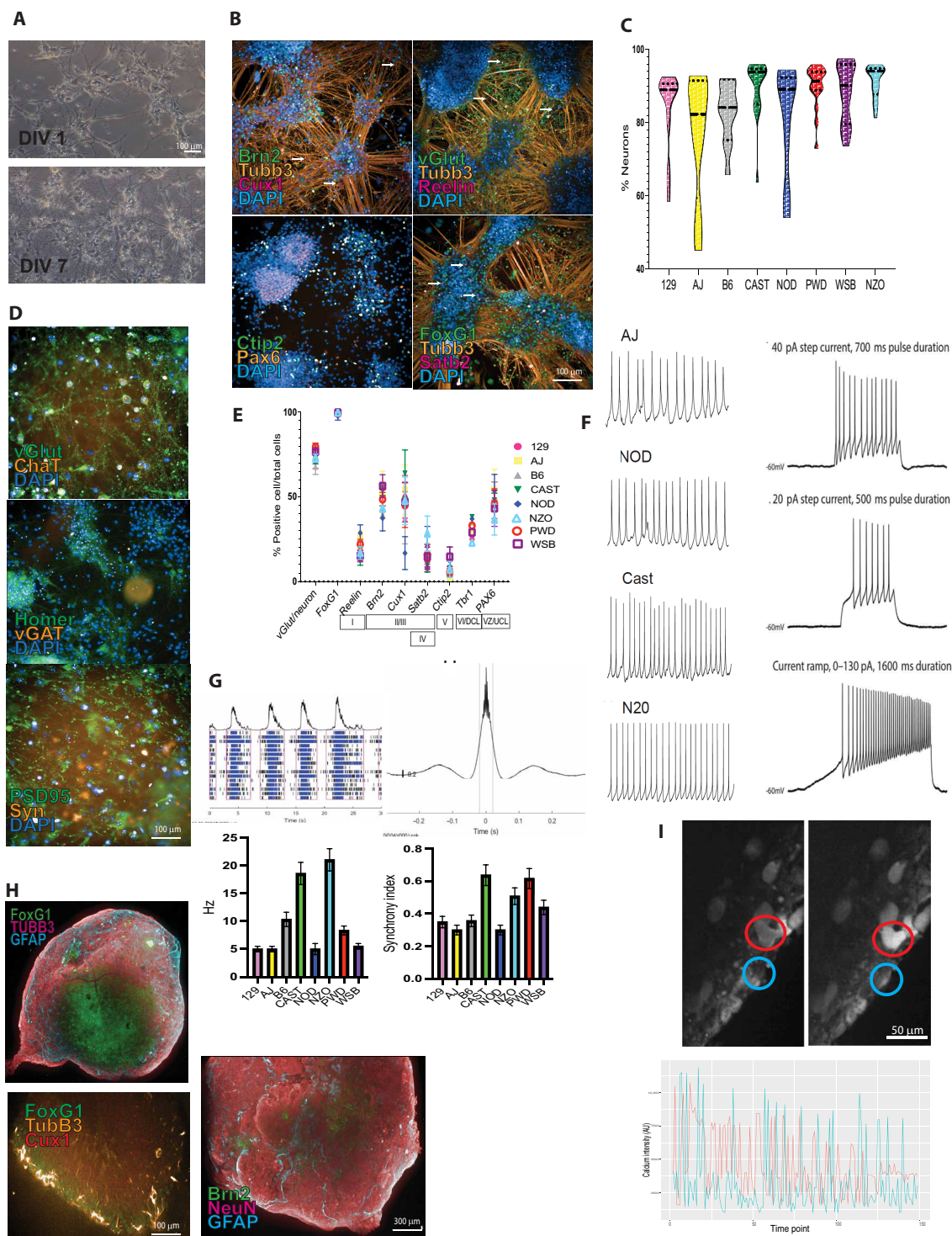
Fig. 1. mESC-derived NPCs follow the default differentiation pathway into cortical neurons and cortical cerebral organoids. (A) Neurons start to develop processes 1 day after seeding, and they become more convoluted after 7 days. **(B)** Immunostaining for different cortical layer markers. **(C)** Violin plot showing the percentage of mESC-derived neurons for each of the eight different mESC strains studied. **(D)** Immunostaining for neurotransmitters and synaptic markers. **(E)** Plot showing glutamatergic, forebrain, and cortical layer markers from all the strains of mESC-derived neurons. Data are represented as means ± SEM. **(F)** Representative images of whole-cell patch clamp neuron recordings, spontaneous activity on the left and evoked potentials on the right. **(G)** Representative recordings of mESC-derived neurons on MEA plates. Top left: Raster plot. Top right: A representative image of synchrony within the well. Bottom left: Column plot showing spike activity (hertz) among the neurons derived from all strains. Bottom right: Synchrony index among the neurons derived from all strains. Data are represented as means ± SEM. **(H)** Representative images of mESC-derived organoids showing different cortical markers. **(I)** Top, calcium imaging of mESC cerebral organoids. Circles show two examples of cells with changes in calcium activity. Bottom: Plot showing the activity of the two cells in the top panel followed through time. DIV, days in vitro; DAPI, 4′,6-diamidino-2-phenylindole.
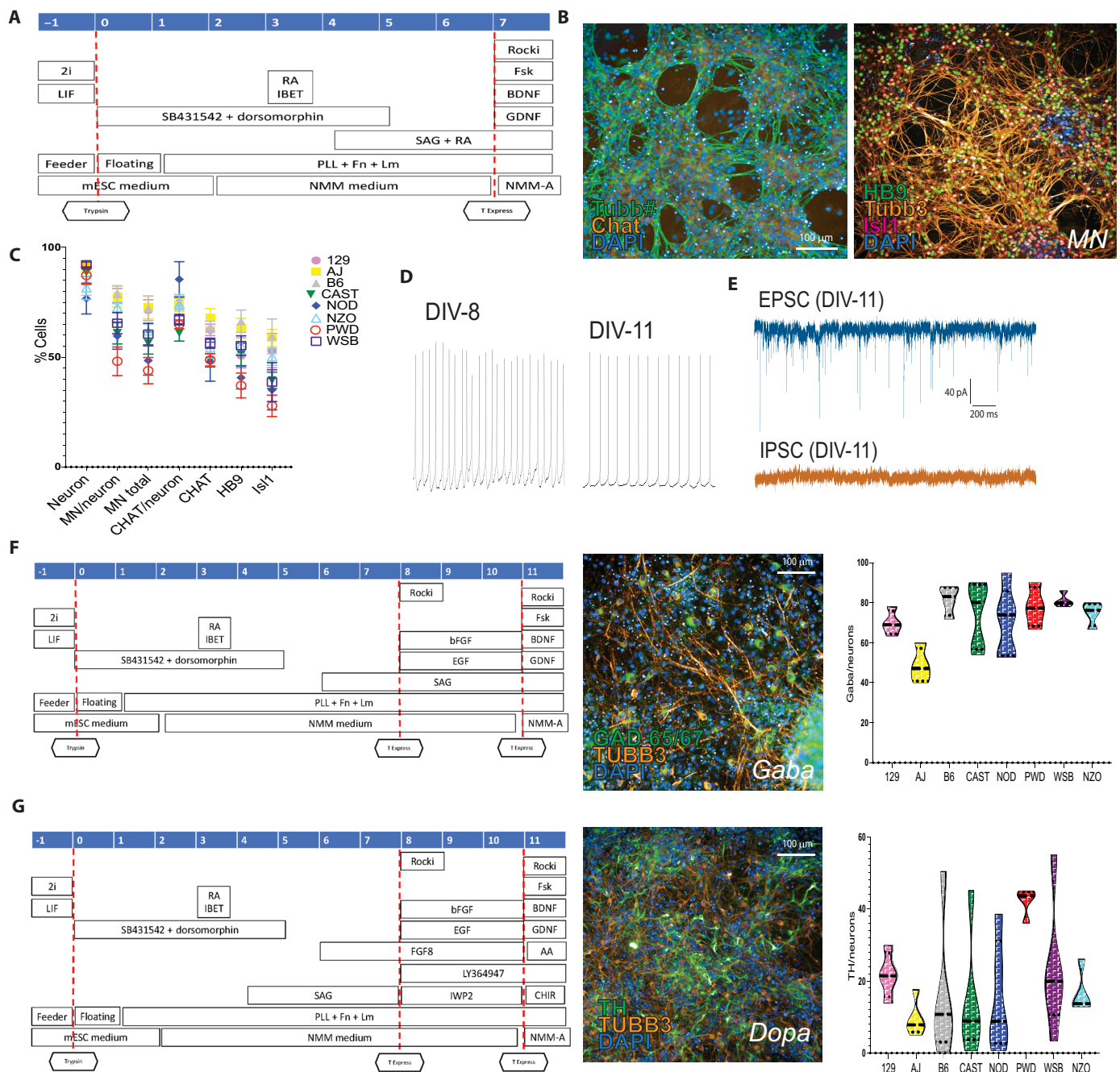
Fig. 2. Generation of specific neuronal subtypes by molecular patterning. (**A**) Scheme of the differentiation protocol to generate mESC-derived MN. (**B**) Immunostaining for MN markers. (**C**) Plot showing the differentiation efficiency to motor neurons among the eight mESC strains. Total neurons were estimated by Tubb staining and motor neurons by the expression of HB9 and/or ISL1; HB9 is a generic marker of motor neurons, ISL1 marks a subset of spinal motor neurons, and CHAT is expressed in mature motor neurons. Data are represented as means ± SEM. (**D**) Whole-cell patch clamp recording performed at days 8 (left) and 11 (right) of the MN differentiation. (**E**) Representative EPSC and IPSC recordings on mESC-derived MN. (**F**) Scheme of the differentiation protocol to generate mESC-derived GABAergic neurons (left) with a representative image of GABAergic neurons (center) and quantification of the differentiation efficiency among all mESC tested (right). (**G**) Scheme of the differentiation protocol to generate mESC-derived dopaminergic neurons (left) with an image of dopaminergic neurons (center) and quantification of the differentiation efficiency among all mESCs tested (right).
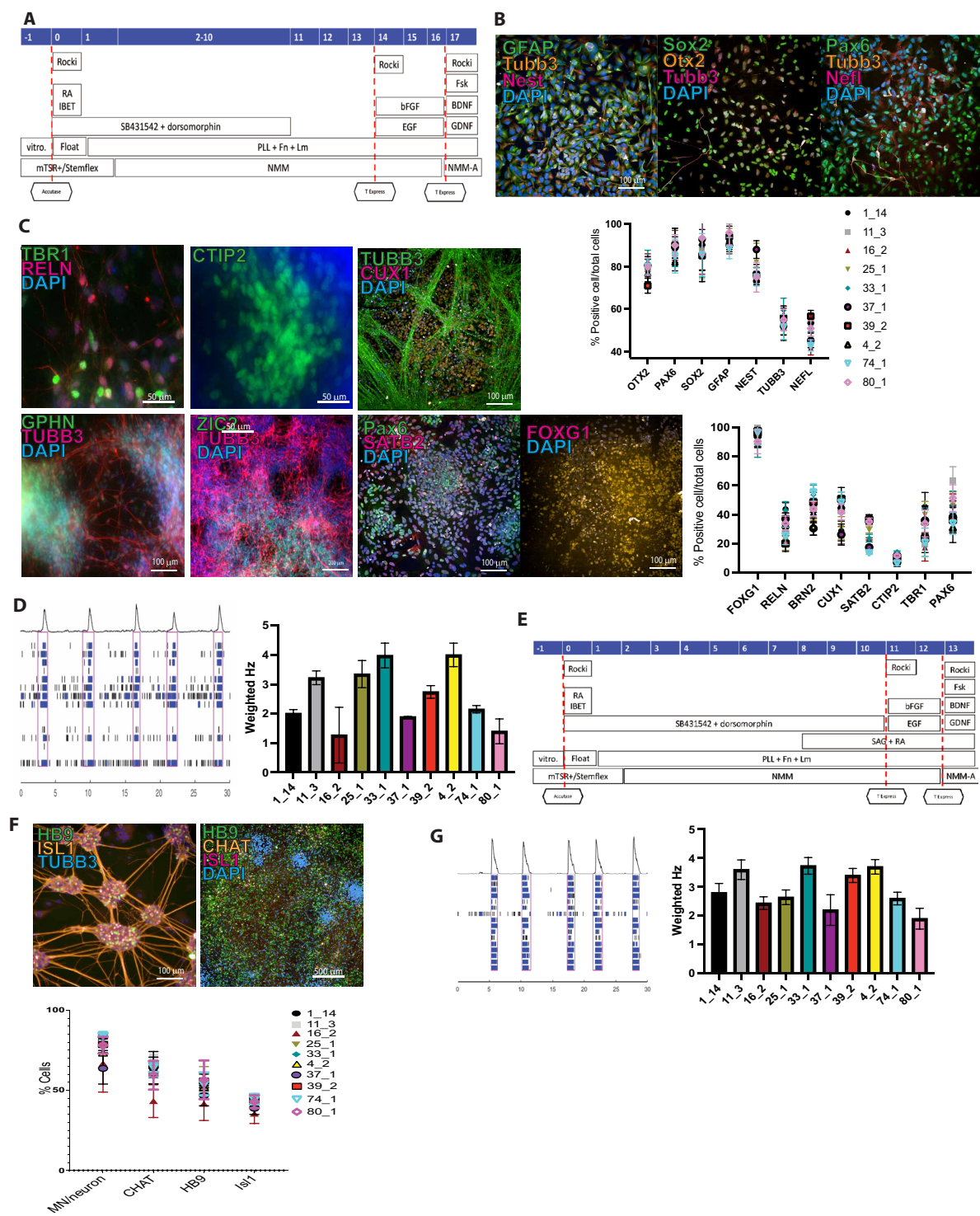
Fig. 3. Genetically diverse hPSC can be differentiated into cortical and MN. (**A**) Scheme of the differentiation protocol to generate hPSC-derived cortical neurons. (**B**) Immunostaining of hPSC-derived NPC and quantification of NPC markers (bottom). Data are represented as means ± SEM. (**C**) Cortical layer markers after 3 weeks of maturation and quantification (right). Data are represented as means ± SEM. (**D**) Representative raster plot of hPSC-derived cortical neurons obtained using an MEA plate after 3 weeks of maturation (left). Quantification of frequency among the 10 genetically diverse iPSCs (right). (**E**) Scheme of the differentiation protocol to generate HPSC-derived MN. (**F**) Representative images of hPSC-differentiated MN showing phenotype-related markers (top) and quantification efficiency among the 10 genetically diverse iPSCs (bottom). (**G**) Representative raster plot of hPSC-derived MNs obtained using an MEA plate after 3 weeks of maturation (left) and quantification of frequency among the 10 genetically diverse iPSCs (right).

plus PD0325901 and CHIR99021, optimal maintenance of naïve state mESC, (*38*)], LIF + ID-8, LIF, and ID-8. These cell lines were previously shown to vary in their response to LIF and in the stability of the undifferentiated state (*15*, *39*); some lines remain in the undifferentiated state, and others switch on lineage markers as soon as LIF + 2i optimal conditions are abandoned, especially those mESC lines from strains regarded to be recalcitrant to stem cell derivation (*14*).

Using HCS, we analyzed the expression of 10 different pluripotency and lineage-specific markers during 4 days of culture in the above conditions (Fig. 4, A and B). Only LIF + 2i was able to maintain the expression of the pluripotency-associated factors POU5F1, NANOG, and SOX2 in all cell lines; nonetheless, PWD and NZO expressed these markers at low levels under all conditions. ID-8 was originally found to substitute for LIF in mESC maintenance on the 129 background (*33*). Comparing cultures grown in LIF + 2i with ID-8, we note that 129, AJ, and B6 show the best maintenance of NANOG expression in ID8 alone (Fig. 4B, bottom). We also examined the proportion of cells expressing markers of the three embryonic germ layers (Fig. 4B, top). Those cell lines that showed consistent expression of pluripotency markers in ID-8 also showed low expression of most germ layer lineage markers. Colony morphometry using HCS provides another indicator of cellular response to the culture environment. Loss of stem cell marker expression generally correlated with changes in colony morphology, as morphometry showed that cell colonies became less compact and circular in ID-8 alone, and LIF + ID-8 enhanced roundness in 129 only (Fig. 4C). Comparing LIF versus ID-8 alone, the two conditions maintain pluripotency-associated markers to a similar degree, but in 129, B6, and CAST, mesodermal markers are expressed at higher levels (Fig. 4, B and D). In summary, these results confirm previous studies in 129 mESC and hPSC, indicating that DYRK1A inhibition can help maintain the undifferentiated state. AJ- and B6-derived mESCs respond to ID-8 similarly to 129, but strains that are poorly maintained in LIF + 2i are not rescued by DYRK1A inhibition.

DYRK1A inhibition differentially blocks neural progenitor proliferation in a strain-dependent fashion

Next, we used our differentiation system to study multiple stages in neural development, from neural lineage specification through to neurogenesis, neuronal differentiation, and maturation. For this, we differentiated the eight mESC lines into NPC using our protocol in the absence or presence of ID-8 and analyzed the cultures at the beginning and on days 2, 5, and 8 via immunostaining and HCS (Fig. 5, A and B). Following induction of neural specification in the presence of ID-8, B6 cultures contained lower percentages of OTX2 and TUBB3-positive cells and displayed a marked reduction in the proportion of KI67-positive cells compared to control. Inhibition of the proliferation of NPCs during development is a hallmark of *Dyrk1a* haploinsufficiency. Further examination of the proliferation of neural progenitors from additional mESC clones of B6, AJ, 129, and WSB using KI67 and MCM2 immunostaining confirmed that the proliferation of B6 cells was strongly inhibited by ID8, whereas the latter three strains were unaffected (Fig. 5, C and D).

We previously observed an inhibition of neural specification in hPSC similar to that noted here (*36*). We therefore examined the effect of heterozygous loss of *DYRK1A* on neural progenitor proliferation in the human-induced PSC (hiPSC) line KOLF2.1J (*40*). The susceptibility of B6 NPCs to inhibition of proliferation by ID-8 was

mirrored in the reduced growth of $DYRK1A^{+/-}$ human iPSC neural progenitors relative to controls (Fig. 5E). Thus, in terms of effects of DYRK1A inhibition on the maintenance of the undifferentiated state, interference with neural specification, and reduction of neural progenitor proliferation, the B6 mESC display the best face validity for modeling the response of hPSCs to DYRK1A inhibition or haploinsufficiency.

To corroborate that the observed neural differentiation impairment is caused by ID-8–induced DYRK1A inhibition, we generated *Dyrk1a* knockout mESC lines, specifically on B6, 129, and WSB backgrounds. We conducted NPC differentiation on these cell lines and analyzed the phenotype. Similar to results with chemical knockdown of DYRK1A, we observed that the only strain severely affected by *Dyrk1a* deletion was B6, while neural progenitor specification, proliferation, and differentiation in WSB and 129 cell lines were indistinguishable from parental controls (Fig. 6, A and B). During B6 knockout cell line differentiation, we observed a decreased expression of proliferation and neural markers and a decreased number of cells (Fig. 6, A and B). The proportion of cells expressing DYRK1A, and the intensity of staining, was similar in wild-type (WT) cells of all three strains (Fig. 6B).

Although all strains had different degrees of response to ID-8 during neural progenitor specification and expansion, WSB was the most unresponsive, while B6 was the most affected. Bulk RNA-seq was performed on these two cell lines at day 8 of differentiation to identify the differences in gene expression associated with the extreme phenotypic differences found between WSB and B6. This difference in response to the inhibitor is evident from the numbers of differentially expressed genes (DEGs); there were more than 700 DEGs between B6 control and ID-8–treated cultures, but only 13 for control versus treated WSB (Fig. 7A).

Regulatory transcriptional network analysis (RTNA) revealed *Foxb1*, *Hoxa4*, and *Hoxd3* as the top regulons associated with the differences found between WSB and B6 in response to ID-8 treatment (Fig. 7B). *Foxb1* is a regulator of neural progenitor differentiation (*41*) and is rapidly and transiently induced during cortical specification of hPSC (*42*). The two Hox genes are associated with hindbrain patterning in the CNS (*43*). These pathways, not previously associated with *Dyrk1a* loss, are consistent with interference in neurogenesis and specific perturbations in hindbrain development (reported below) associated with *Dyrk1a* haploinsufficiency.

Gene ontology (GO) analysis indicated that either under control conditions or in the presence of ID-8, DEGs associated with the response to LIF were highly overrepresented in B6 versus WSB (Fig. 7C, left). The LIF signaling pathway is responsible not only for maintenance of mESC but also for the maintenance of mouse neural stem cells in vitro and in vivo (*44*) and enhances the proliferation of human outer radial glial cells (*45*). In the presence of ID-8, DEGs associated with the GO term synaptic membrane were overrepresented in WSB relative to B6 (Fig. 7C, right), consistent with progression of neural differentiation in the former but not the latter.

Using the RNA-seq data, we also analyzed gene isoform changes due to treatment and between B6 and WSB strains. Isoform usage can change considerably even when there is no overall change in gene expression, with functional consequences (*46*), and *Dyrk1a* is known to regulate the activity of a number of RNA splicing proteins (*47–50*). Global analysis showed that adding ID-8 induced a loss of exons in B6 strain but not in WSB (Fig. 7D). We found 200 unique genes with alternative isoform usage when control B6 cells were compared to WSB
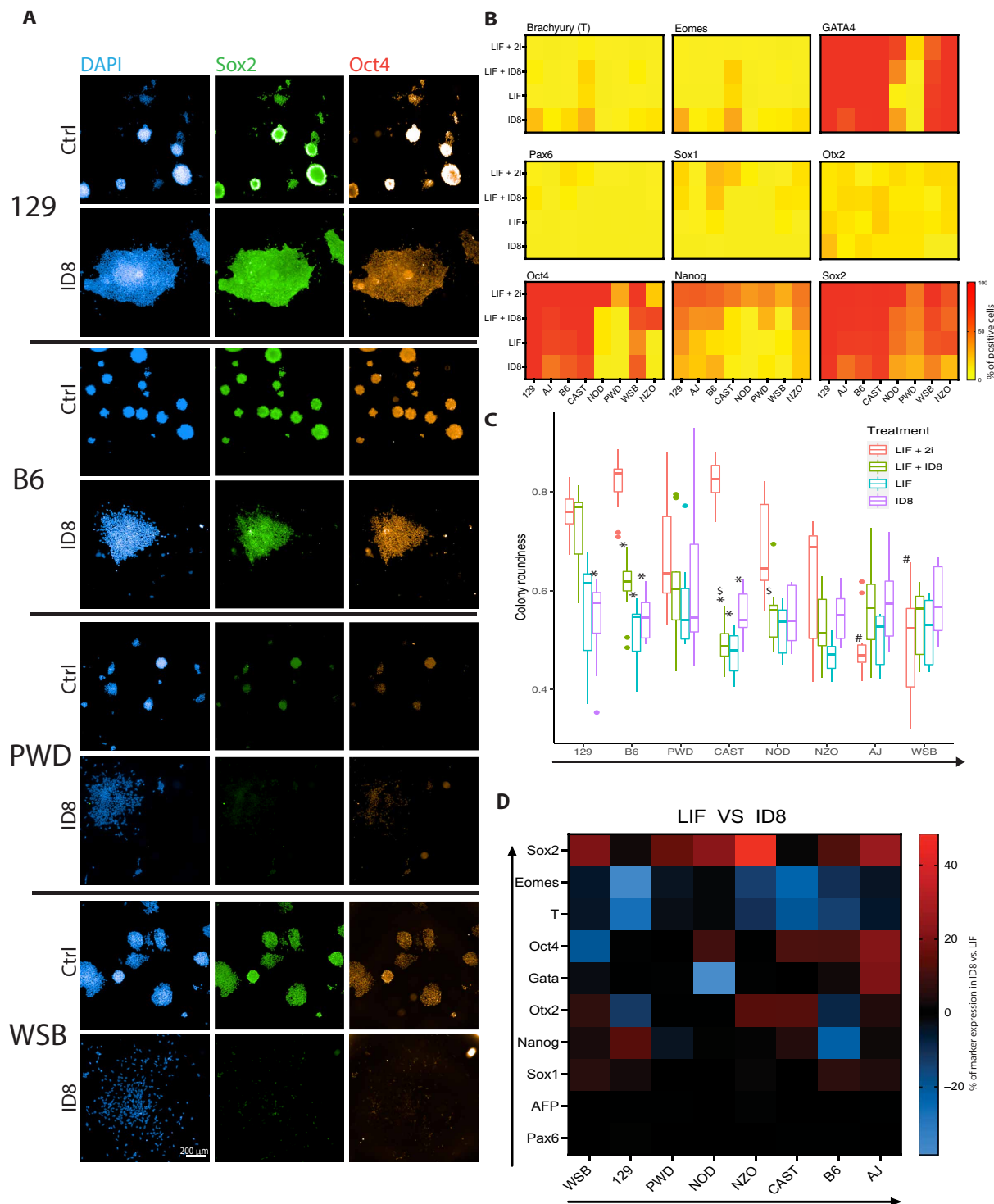
Fig. 4. Effects of DYRK1A inhibition on mESC maintenance and lineage specification vary across genetically diverse mouse strains. (A) Immunofluorescence images showing immunostaining for pluripotency markers in the eight different CC founder mESC cultured in four different culture conditions for 4 days. (**B**) Heatmaps showing the percentage of cells expressing the markers in the mESC as measured by HCS. (**C**) Morphometry analysis of the mESC colonies. (**D**) Heatmap comparing the effects of LIF versus ID-8 treatment on the overall proportion of cells expressing the analyzed markers in the eight different mESCs, determined by HCS. Red indicates decreased percentage of cells expressing the associated marker in ID8 compared to LIF; green means higher expression. Cell lines and markers are arranged according to the overall degree of change (arrows). * represents statistically significant differences against the control condition (LIF + 2i) within the same cell line. # represents statistically significant differences among cell lines treated with 2i + LIF and compared to the standard cell line 129. $ represents statistically significant differences among cell lines treated with 2i + ID8 and compared to the standard cell line 129. Significant difference is indicated when $P < 0.05$. Means ± SEM are shown. Kruskal-Wallis and Dunn's test were conducted. $n = 4$ biological replicates.
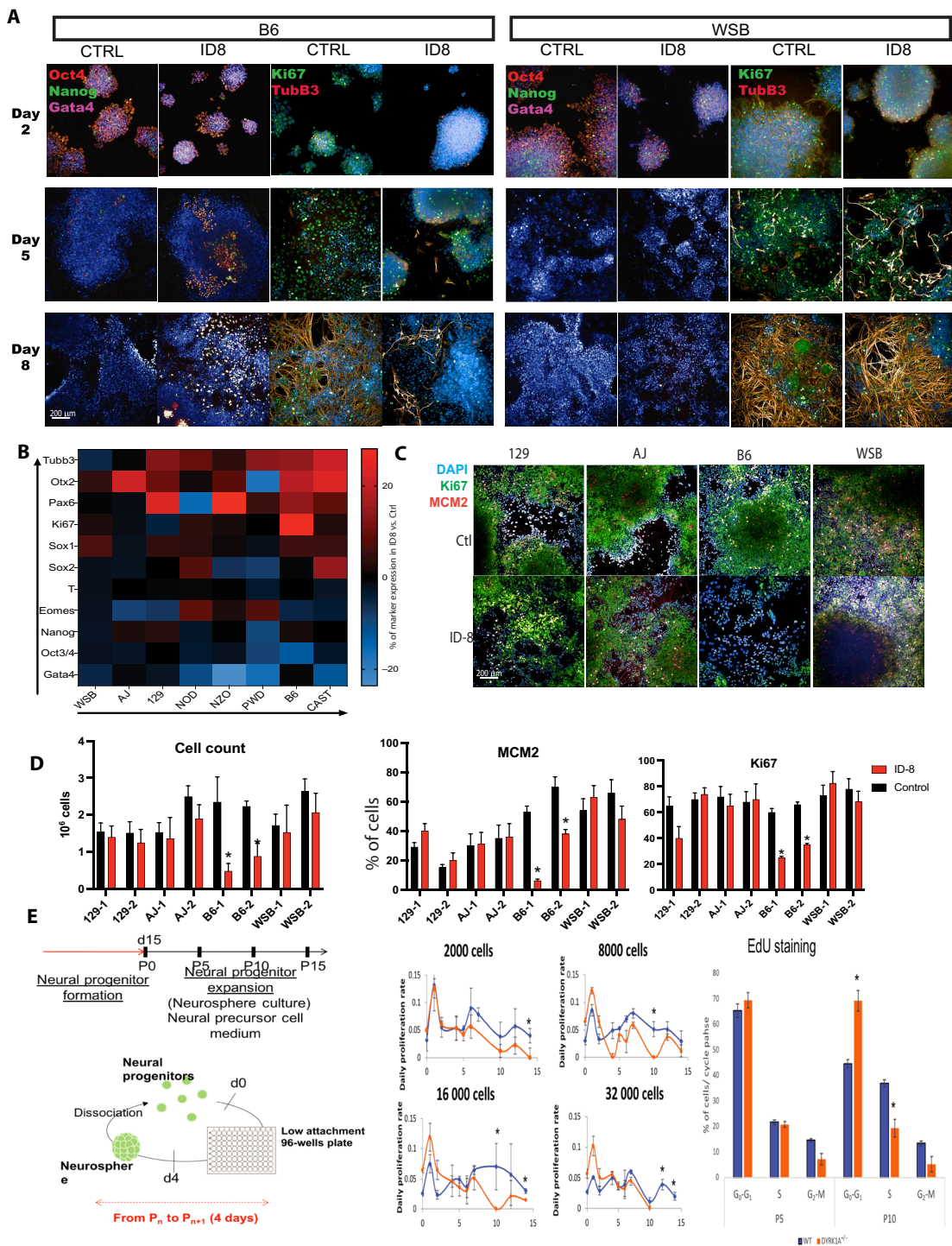
Fig. 5. DYRK1A inhibition differentially blocks neural progenitor proliferation in a strain-dependent fashion. (**A**) Representative images of the B6 and WSB mESC lines differentiated into NPC in the presence of the DYRK1A inhibitor ID8 and analyzed at days 2, 5, and 8. (**B**) Comparison between the proportion of cells expressing the indicated markers as measured by HCS in control and ID-8–treated cells after 8 days of differentiation. Red indicates decreased percentage of cells expressing the associated marker in ID-8–treated cells compared to control, whereas green means an increase. Cell lines and markers are arranged according to the overall degree of change (arrows), and $n = 4$ biological replicates. (**C** and **D**) Images and plots representing the cell count of proliferating NPCs derived from six independent cell lines different from those used in (B). NPCs were cultured with or without ID-8 for five passages. B6 showed a decreased number of cells and proliferative markers (Ki67 and MCM2) compared to its control, whereas 129, AJ and, WSB were not affected. $n = 4$. *Statistically different from its control, $P < 0.05$. Kruskal-Wallis and Dunn's test were conducted. (**E**) Long-term proliferation assay in hPSC-derived NPC. Left: Experimental design [cells were kept in proliferative conditions as neurospheres for 15 passages (2 months total)]. Middle: Cell numbers over time. Right: Percentage of cells in each cycle phase measured by EdU staining in WT and $DYRK1A^{+/-}$. Experiment shows that $DYRK1A^{+/-}$ NPC undergo quiescence faster than control. Two-tailed t test, $n = 4$, *$P < 0.05$.
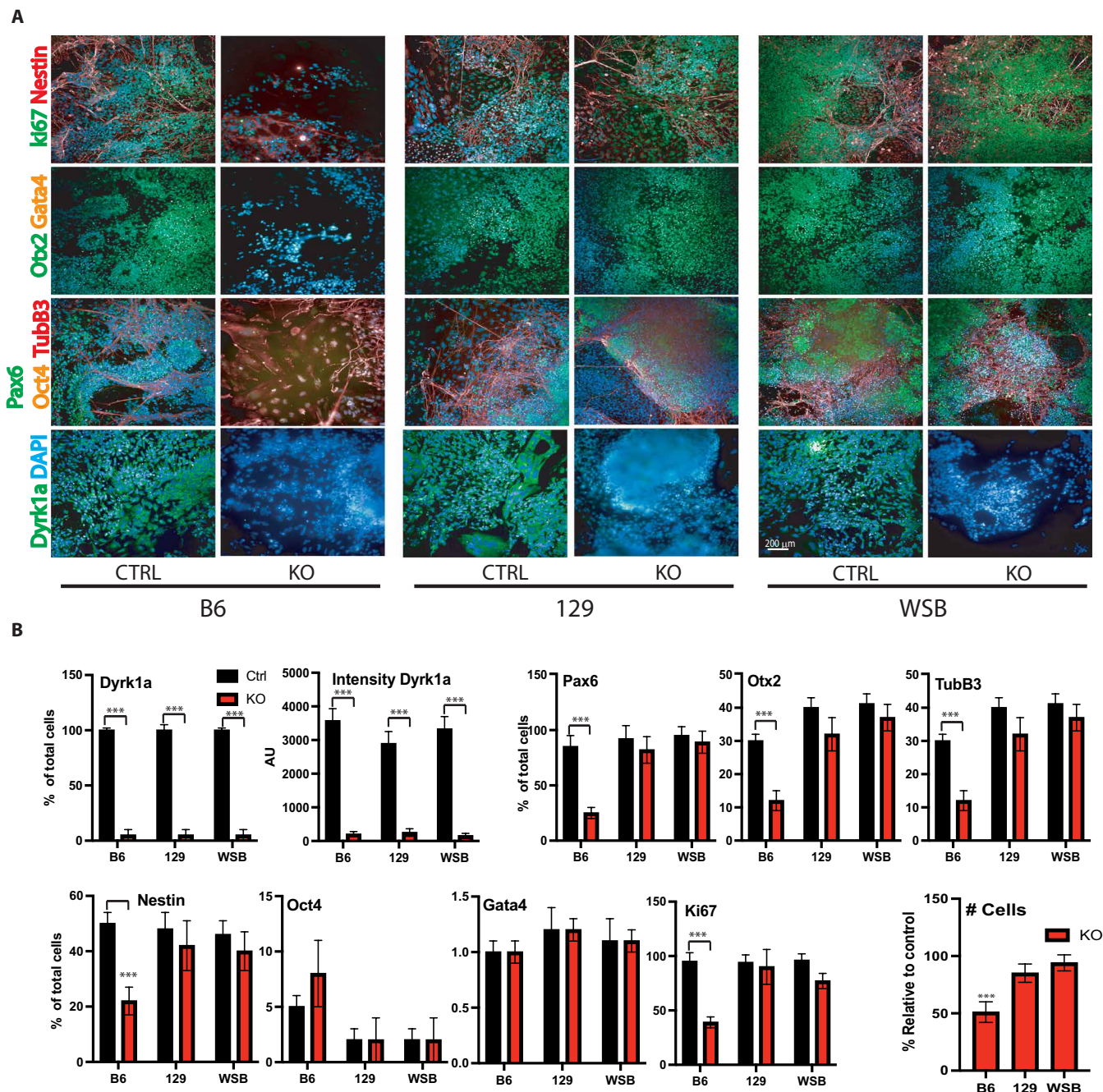
Fig. 6. Neural differentiation of WT and *Dyrk1a*-knockout mESC. (**A**) Representative images at day eight of NPC differentiation showing robust differentiation in 129 and WSB but B6 *Dyrk1a*-knockout. (**B**) Quantitation of proportion of cells expressing DYRK1A (and average intensity of DYRK1A staining) and markers of neural differentiation, pluripotency, and proliferation, measured by immunostaining and HCS in the three strains. Kruskal-Wallis and Dunn's test were conducted. ***$P < 0.05$ compared to its own control $n = 3$ biological replicates.

cells; an increase of variant isoforms between the two strains was observed in the presence of ID-8 (Fig. 7E). Of particular interest was the finding that *Ntrk2* underwent a change in isoform expression in B6 NPC when treated with ID-8, whereas in WSB, these isoforms remained unchanged (Fig. 7F). *Ntrk2* codes for a neurotrophic receptor that binds brain-derived neurotrophic factor (BDNF). We found that ID-8 treatment induces a switch from the canonical isoform to an

isoform lacking the kinase domain. This isoform is unable to transduce signaling via tyrosine phosphorylation, and it is notable that BDNF signaling was implicated in the response to *Dyrk1a* haploinsufficiency in a recent proteomics study in B6 mice (*51*). That study did not investigate alternative splicing, but the results are compatible with our findings.

These results suggest that, in the B6 strain in which neurogenesis is affected, DYRK1A inhibition interferes with multiple pathways
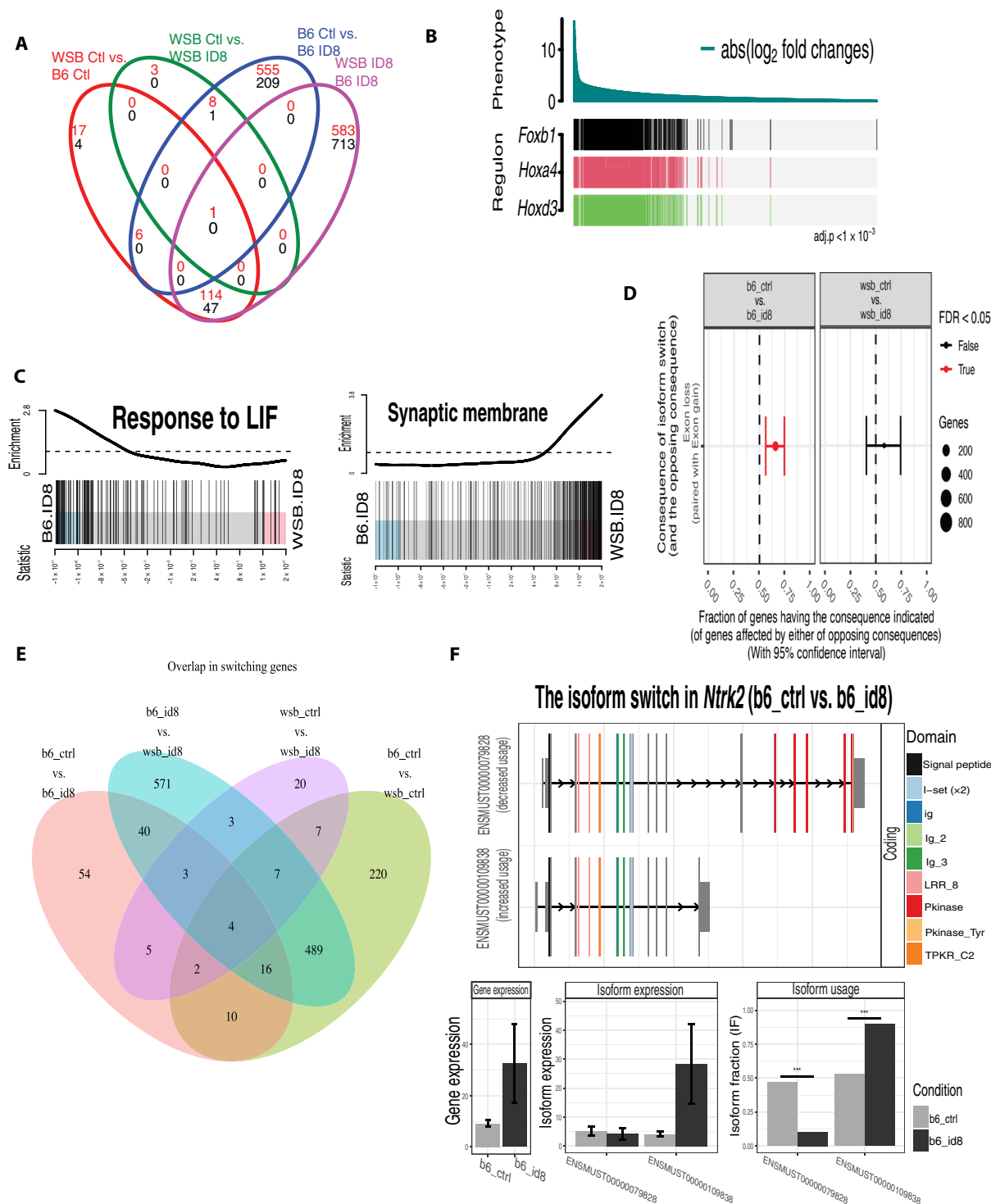
Fig. 7. RNA-seq analysis reveals the genes associated with the impairment in neural induction in B6-derived NPCs. (**A**) Venn diagram of DEG for each set of comparisons. Number in red represents down-regulated genes; black indicates up-regulated gene. (**B**) RTNA for the top regulons associated with differences in ID-8–treated WSB- and B6-derived NPCs. (**C**) Barcode plots showing two exemplary GOs differentially affected in WSB and B6 when treated with ID-8. Genes are ranked from left to right by increasing log fold change represented by the vertical bars. The curve shows the relative local enrichment of the bars in each part of the plot. (**D**) Consequences of isoform switch showing a lost of exons in ID-8–treated B6 neurons. (**E**) Venn diagram showing the global isoform switch differences in B6 versus WSB neurons when treated with ID-8. (**F**) Switch in the *Ntrk2* isoform usage when B6 is treated with ID8. Top plot shows the color-coded domains present on each exon (bars). Bar plots indicating total gene expression, isoform expression, and relative isoform usage proportional to the total gene expression. FDR, false discovery rate.

involved in neural specification, patterning, and differentiation. RNA-seq confirmed the resilience of WSB against, and susceptibility of B6 to, DYRK1A inhibition at the neural induction stage. Subsequent analysis highlighted key pathways in neurogenesis downstream of DYRK1A inhibition and identified a profound effect of DYRK1A inhibition on mRNA isoform usage. In the case of BDNF signaling, our results implicated alteration of isoform usage as an important genetic determinant of the response of neural progenitors to chemical knockdown.

DYRK1A inhibition delays functional maturation of neurons and modulates gene expression of maturation-related genes in a strain-dependent fashion

To understand how DYRK1A inhibition modulates physiological maturation of neurons, we used MEA plates capable of recording 16 field potentials per well on a 48-well plate to assess electrophysiological activity. We seeded young neurons and let them mature for 6 weeks while analyzing electrical activity at different time points (Fig. 8, A and B). Addition of ID-8 began 2 days after the NPCs were seeded and continued throughout.

All cell lines were capable of generating action potentials and bursts of spikes, and creating networks, but not all cell lines matured at the same rate. CAST, B6, and 129 were the cell lines that matured the fastest, measured by hertz, bursting activity, and synchrony, while PWD took the longest (Fig. 8, A and B). We found that in most of the strains, addition of ID-8 inhibited the development of electrical activity; neurons fired less, and bursts of activity were less frequent. Complementarily, interburst intervals, the relative silent time between two trains of activity, were longer for most cell lines when ID-8 was added. Quantitative analysis of a range of parameters at the peak point of control electrical activity (Fig. 8B) confirmed inhibition of maturation across most strains by measurement of mean firing rate, number of bursts, prolongation of interburst intervals, and a reduction in spikes per burst. Two overall patterns were observed. In B6, CAST, A/J, and NOD, maturation was delayed and suppressed throughout the time course, while in PWD, 129, NZO, and WSB, maturation was delayed, but activity recovered at the later time point (Fig. 8, B and C). Together, once again, the functional maturation of neurons from B6 mESC was sensitive to ID-8, that of WSB mESC-derived cells were partially resistant to ID-8, and NZO-derived neurons were the most resilient among all the strains. A decreased rate of functional network maturation is consistent with known effects of ID-8 on axonal growth and dendrite arborization.

We next performed RNA-seq on WSB and B6 neurons. Analysis at this stage showed a similar pattern to the NPC stage on the multidimensional scaling (MDS) plot, which separates the neurons by strain and treatment; it also showed more distance between B6 subgroups than the WSB counterpart, indicating that B6 was more affected by DYRK1A inhibition (fig. S6A). After ID-8 treatment, there were 220 DEGs between WSB and B6 (fig. S6B). GO analysis of DEG differentially affected by ID-8 in the two strains identified biological adhesion and transmembrane receptor signaling, with WSB showing a greater enrichment following ID-8 treatment (fig. S6C). Cellular adhesion molecules are important for neural development and axonal growth (52). *Rxrg*, *Dmrtb1*, and *lrf7* were the top regulons associated with the differences in response to DYRK1A inhibition between WSB and B6 neurons (fig. S6D). *Rxrg* has been associated with neurodegeneration (53), and *Irf7* is a key mediator of the innate and adaptive immune responses (54) and positively regulates microglia polarization to the M2 state.

As we observed during neurogenesis, we also found more alternative splicing events in B6 compared to WSB neurons when treated with ID-8 (fig. S6E). An example of this is *Slit2*, which exhibited isoform switches in B6 neurons when treated with ID-8 (fig. S6F). *Slit2* is associated with axonal guidance, cell migration, and arborization (55). All these developmental processes are affected by Dyrk1a mutations (56, 57).

mESC strain differences in recovery from axonal injury in vitro reflect genetics of recovery from brain injury in vivo

There are marked strain differences in the ability of different mouse strains to respond to injury to the CNS (58). Abundant evidence confirms that *Dyrk1a* plays a role during neurite sprouting in normal development and that gene dosage alteration affects axonal growth and dendrite arborization (24), but it is not known whether these developmental roles of *Dyrk1a* might be recapitulated during axonal regeneration. As a further test of the predictive power of our in vitro system, we performed axotomy to analyze differences in axonal regrowth in neurons derived from mESC from CC founder strains.

We differentiated the mESC into neurons and cultured them into microfluidic chambers (Fig. 9A). On these devices, neurons were seeded on one chamber; axons could traverse microgrooves reaching into a second chamber, whereas somas could not. After 4 days, axons grew through to the second chamber (Fig. 9B). However, the number of axons growing through to the second chamber, and their length and density, indicated by the total area occupied by axons, varied among mESC strains (Fig. 9C). At this point, axons were cut off and left to recover for four more days while being treated or untreated with ID-8. In all cases, under control conditions, more axons grew across the device and had longer processes than before injury, except for B6 neurons (Fig. 9, B to D). CAST, NOD, and NZO grew considerably more following injury compared to all other strains. When ID-8 was added, most of the lines showed less growth than controls. WSB, AJ, and PWD axons occupied the same area after regrowth in the presence of ID8 as the control did (Fig. 9D). WSB axons experienced the longest growth before and after injury (both control and ID-8 treated). Notably, the extent of axon growth before injury was not predictive of the extent of regrowth after injury (e.g., 129 versus NZO versus B6; Fig. 9C).

Because of this divergent response to injury between B6 and WSB, we again undertook bulk RNA-seq analysis on these two cell lines to identify the underlying transcriptional differences. MDS analysis demonstrated vastly different responses between the two strains in the response to axotomy in the presence or absence of ID-8. As we saw from experiments in the maturation stage, ID-8 affected the transcriptome in both strains in control or axotomized cultures. However, when axons are severed, the B6 transcriptome showed limited change, irrespective of ID-8 treatment, whereas WSB transcriptome shifts markedly in response to axotomy in control and ID-8–treated cultures. The combination of ID-8 and axotomy displays an additive effect on the transcriptome in WSB, whereas in B6, this response is not observed, as axonal cut with or without ID-8 ("no drug") elicits the same effect (Fig. 9E).

When axons were cut, the two cell lines (B6 and WSB) expressed a core set of genes. These genes were *Map11*, *Ntsr1*, *Ccn5*, *Slc16a3*, and, *Smtnl2* reflecting GO associated with GO terms cellular response to hypoxia and neuron projection, both being part of a successful neuronal reaction to injury (Fig. 9F). Top regulons for the differences found between the cell lines when injured were *Ascl1*, Creb5,
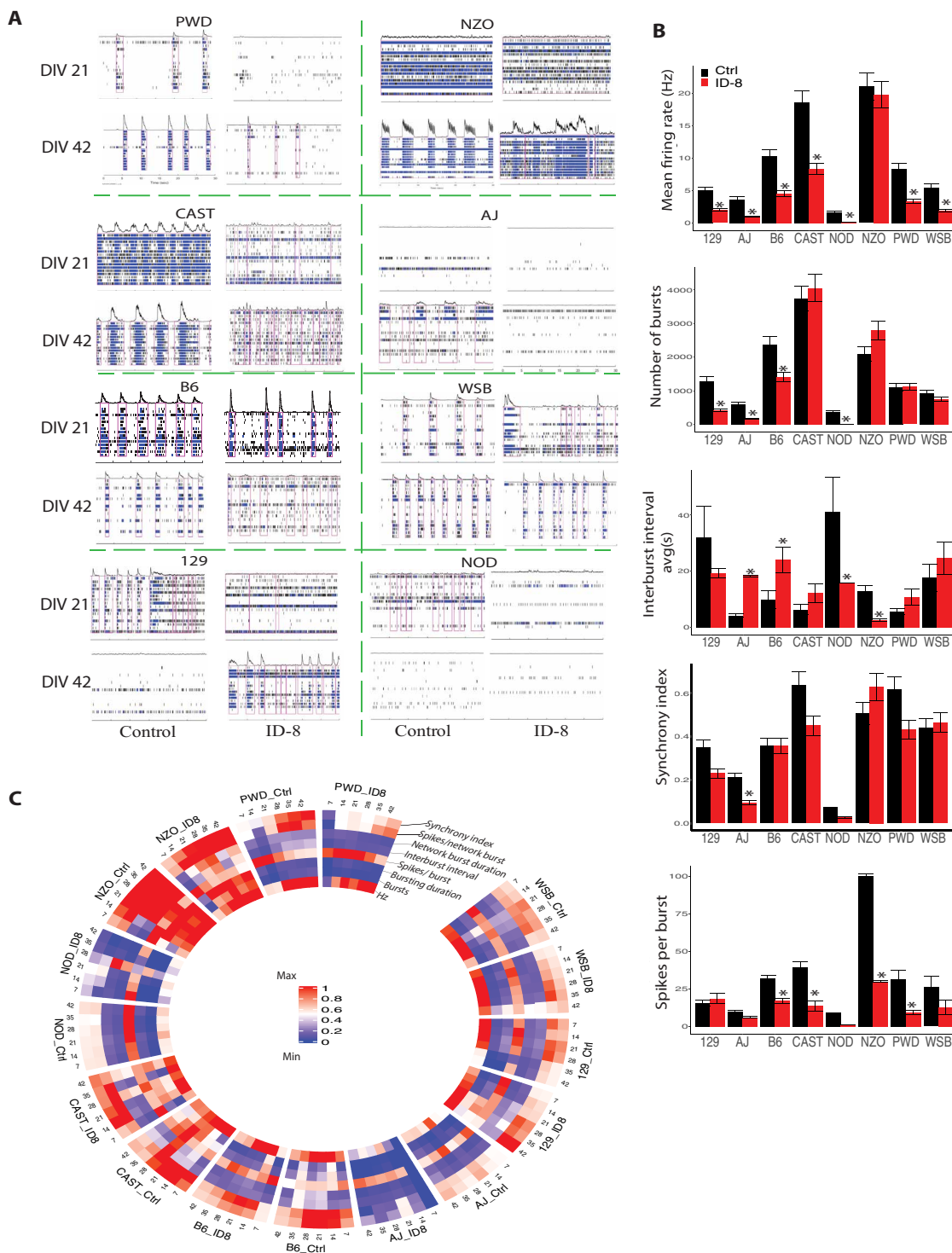
Fig. 8. Effect of DYRK1A inhibition on delays in functional maturation of neurons by mESC strain. (**A**) Examples of 30-s recordings of all differentiated neurons (21 and 42 days in vitro) in the presence or absence of ID-8. (**B**) Plots for firing rate, number of bursts, interburst interval, synchrony, and spikes per burst. Because the neurons from different strains do not mature and survive equally, data form comparisons among the cell lines were taken at the time point where the highest frequency of firing (hertz) was recorded for each cell strain. Means ± SEM are shown. Kruskal-Wallis and Dunn's test were conducted. *$P < 0.05$ compared to its own control, $n = 3$ biological replicates. (**C**) Circular plot showing different electrophysiological properties during 42 DIV in the presence of ID-8.
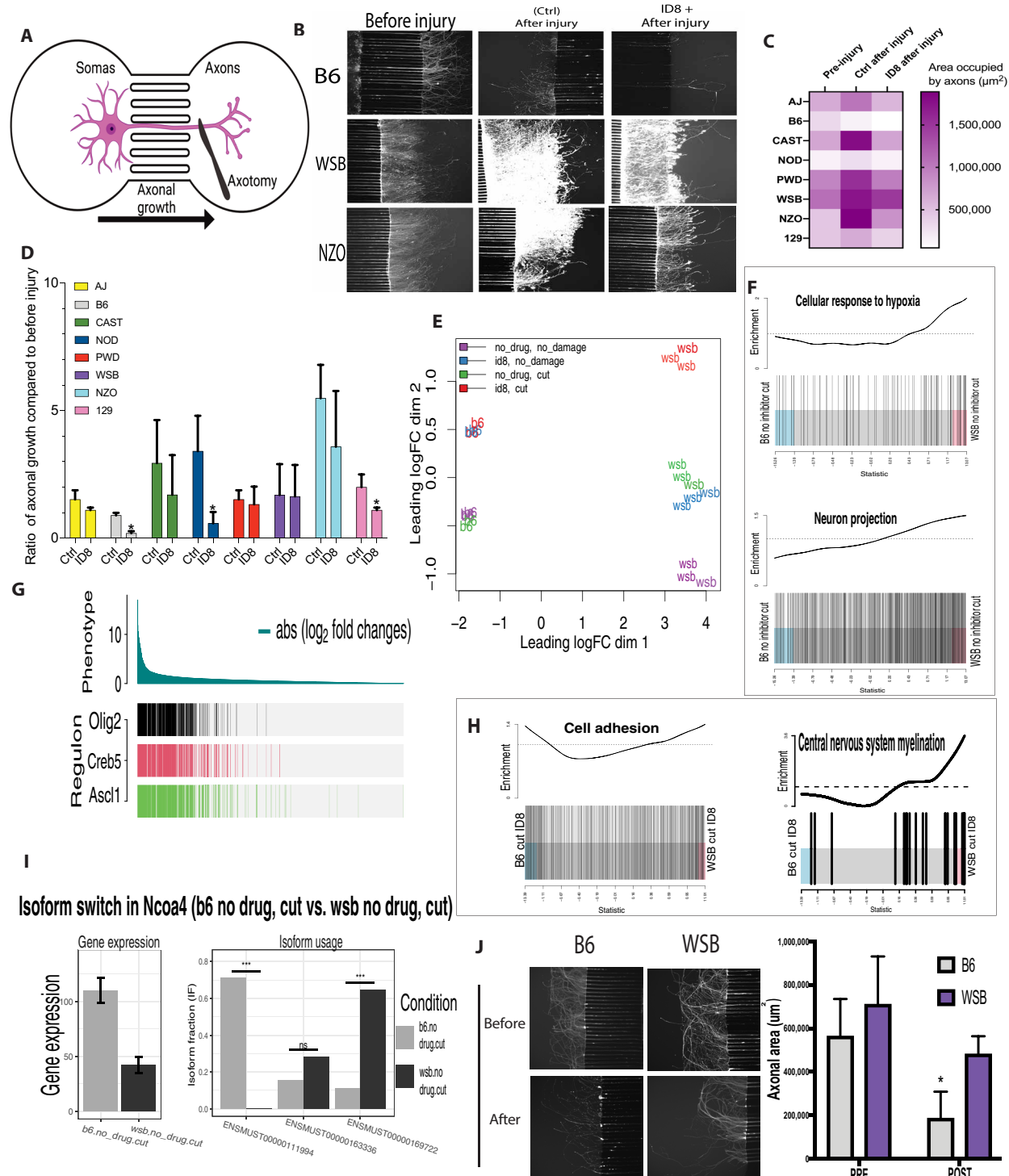
Fig. 9. mESC-derived neuronal strain differences in recovery from axon injury in vitro. (**A**) Illustration of the microfluidic chamber used to isolate axons from somas. Image taken from chamber manufacturer webpage. (**B**) Representative images of B6, WSB, and NZO neurons in microfluidic chambers before injury, after injury in the absence of ID-8, and after injury in the presence of ID-8. (**C**) Heatmap for the area occupied by axons in chamber two (axonal side) before and after injury. (**D**) Ratio of axonal growth compared to pre-injury in both control and treated neurons. Dunnet's test was used for statistical analysis on three biological replicates. (**E**) MDS plot showing the differences between cell lines over all three conditions. (**F**) Barcode plots showing GO analysis of differential response to axonal injury between WSB and B6 in the absence or presence of ID-8. (**G**) RTNA showing the top three regulons associated with the differences between WSB and B6 when axons are injured. (**H**) Enrichment analysis and comparison of isoform switches between the differences in axonal recovery between B6 and WSB treated or not treated with ID8. (**I**) Isoform switch in the *Ncoa4* gene. (**J**) Axonal recovery experiment conducted on isolated primary cortical neurons from B6 and WSB P5 mice. *t* test for statistical analysis on three biological replicates.

and *Olig2* (Fig. 9G). These transcription factors are important for neuronal differentiation and myelination. *Ascl1* has been associated with a superior regenerative capacity in dorsal root ganglion neurons in CAST versus B6 in vivo (*59*). This differential expression pattern only emerged between the two strains after axonal injury.

After axons were cut and treated with ID-8, more genes were differentially expressed in WSB than in B6 (twofold). Top common DEG genes in both cell lines were *Padi2*, *Calcr*, *Itgb4*, *Ifitm1*, *Npy*, *Tnfrsf11b*, *C1ra*, and *Pcolce*; all of them are associated with axonal growth and guidance. In WSB-derived ID-8–treated neurons, gene sets associated with cell adhesion and CNS myelination were upregulated compared to the B6 counterpart (Fig. 9H) and were confirmed by the number of hits per GO. This profile can explain a more robust axonal growth after axonal damage in WSB neurons. Last, RTNA showed that two of the top three regulons associated with the differences in recovery after axonal growth, *Olig2* and *Ascl1*, were similar to those identified in the axonal damage response in the absence of ID-8. These results suggest that *Olig2*, *Creb5*, and *Ascl1* are part of the core regulatory network for a fast axonal growth after axonal damage when B6 and WSB are compared. Isoform-switched analysis unveiled that *Ncoa4* was not only down-regulated but also switched in isoforms found after axotomy (Fig. 9I). *Ncoa4* was recently associated with ferritinophagy and neurodegeneration (*60*). A comparison of axonal regrowth of primary cortical neurons from postnatal 5 (P5) newborn B6 or WSB mice confirmed that the differences in growth after injury seen in mESC-derived neurons reflected the regrowth capacity of neurons isolated directly from the postnatal brain (Fig. 9J).

Using all of the RNA-seq data, we analyzed the effect of ID-8 treatment independently of the cell strain, and also compared across the two strains independently of the treatment, throughout all stages analyzed. Analyzing the effects of ID-8 in a strain-independent fashion, we found only 15 DEGs, but the cross-strain comparison independent of treatment found 261 DEGs (fig. S7A). Similar to the gene expression differences, differential use of transcript variants were found between strains, and our data indicated that in general, the consequences of isoform switches in B6 resulted in shorter transcripts (fig. S7B). It is worth pointing out that *Gapdh*, a housekeeping gene commonly used to normalize expression data, was differentially expressed between WSB and B6 regardless of treatment (fig. S7C). This disparity could be associated with differences in metabolic demands and energetic substrates. The latter correlates with differences we observed in other ontologies such as mitochondrial respiratory chain complex II assembly and monocarboxylic acid metabolic process (fig. S7D). A gene set more enriched in B6 independently of treatment was the regulation of apoptotic process involved in development, whereas that a cerebral cortex development gene set was differentially affected by ID-8, B6 being more severely affected (fig. S7D). Gene sets enriched in WSB relative to B6 in the presence of ID-8 included genes involved in cortex development, forebrain development, and cell proliferation in the forebrain, all in accordance with differential effects on NPC proliferation in the two strains.

Heterozygous loss of *Dyrk1a* is lethal on the B6 background but not on 129 or A/J

Last, we sought to establish the relationship between the in vitro susceptibility of B6 to DYRK1A inhibition and the in vivo effects of *Dyrk1a* heterozygosity. We generated a null allele of *Dyrk1a* by crossing female mice carrying the germline cytomegalovirus (CMV)–Cre to male *Dyrk1a* mice carrying the conditional allele of *Dyrk1a* (floxed *Dyrk1a*) (Fig. 10). When both strains were on the B6 background, we did not recover any live pups heterozygous for *Dyrk1a* deletion (*Dyrk1a*$^{+/-}$) from this cross (0 of 93). We were able to obtain several mosaic offspring for the floxed and deleted alleles, but crossing male mosaic mice to WT B6 mice did not produce any live *Dyrk1a*$^{+/-}$ pups (0 of 46). Given that the prototype mouse model of *Dyrk1a* haploinsufficiency was maintained on a mixed B6/129 background (*61*) and our finding that B6 neural progenitors were uniquely sensitive to DYRK1A inhibition, we reasoned that mice carrying the deleted allele may survive on a different background. To test this idea, we crossed male mosaic mice to 129S1 female mice and obtained live *Dyrk1a*$^{+/-}$ mice on a mixed 129/B6 background. We then backcrossed *Dyrk1a*$^{+/-}$ mice to 129S1 for six generations and found that heterozygote animals were born at Mendelian ratios. We also mated B6 *Dyrk1* mosaic to AJ females, and live *Dyrk1a* heterozygous pups were born. These results indicate that heterozygous deletion of *Dyrk1a* causes early lethality on the B6 background but does not affect survival on the 129S1 or AJ background.

We further examined the phenotype of *Dyrk1a*$^{+/-}$ mice on the 129B6F1 background. Western blot analyses showed that the level of DYRK1A protein was reduced by half in *Dyrk1a*$^{+/-}$ mice (Fig. 10B). Mutant mice appeared smaller and weighed 25% less than WT littermates during postnatal development and as young adults (Fig. 10, C and D). Likewise, the brains of *Dyrk1a*$^{+/-}$ mice appeared smaller and weighed 30% less than those of control littermates (Fig. 10, E and F), although the brain-to-body ratio was not significantly changed. Brain histology indicated that the reduction in brain size was not uniform across the brain, with the mid- and hindbrain regions showing larger reductions than the cerebral cortex (Fig. 10G). These results corroborate previous findings that heterozygous deletion of *Dyrk1a* in the mouse causes growth retardation and microcephaly, two key clinical features associated with *DYRK1A* mutations in humans. *Dyrk1a*$^{+/-}$ mice on the 129B6F1 background also showed abnormal behaviors. In the open field apparatus, *Dyrk1a*$^{+/-}$ mice were hypoactive compared with WT littermates (Fig. 10H); they also spent less time in the center of the arena than WT littermates (Fig. 10I), suggesting higher levels of anxiety in the mutant mice. Together, these findings confirm that heterozygous deletion of *Dyrk1a* on an appropriate genetic background recapitulates key features of human disease phenotypes and that the B6 genetic background confers extreme sensitivity to the haploinsufficiency syndrome in the mouse.

DISCUSSION

To facilitate genetic analysis in vitro of neural development across a diverse range of mouse genetic backgrounds, we developed a protocol to differentiate PSCs into neurons from genetically diverse mESC and hPSC. We demonstrated the applicability of this model in analyzing the effects of chemical knockdown or genetic ablation of the activity of a key neurodevelopmental gene throughout neurogenesis, neural maturation, and repair, and we were able to show that the knockdown or knockout phenotypes vary markedly depending on the genetic background. Because we were able to adapt the system to hPSC neural differentiation, this platform will enable cross-species comparison of neurodevelopment in 2D or 3D cultures, allowing analysis of defined cell types at a similar developmental stage under identical environmental conditions.
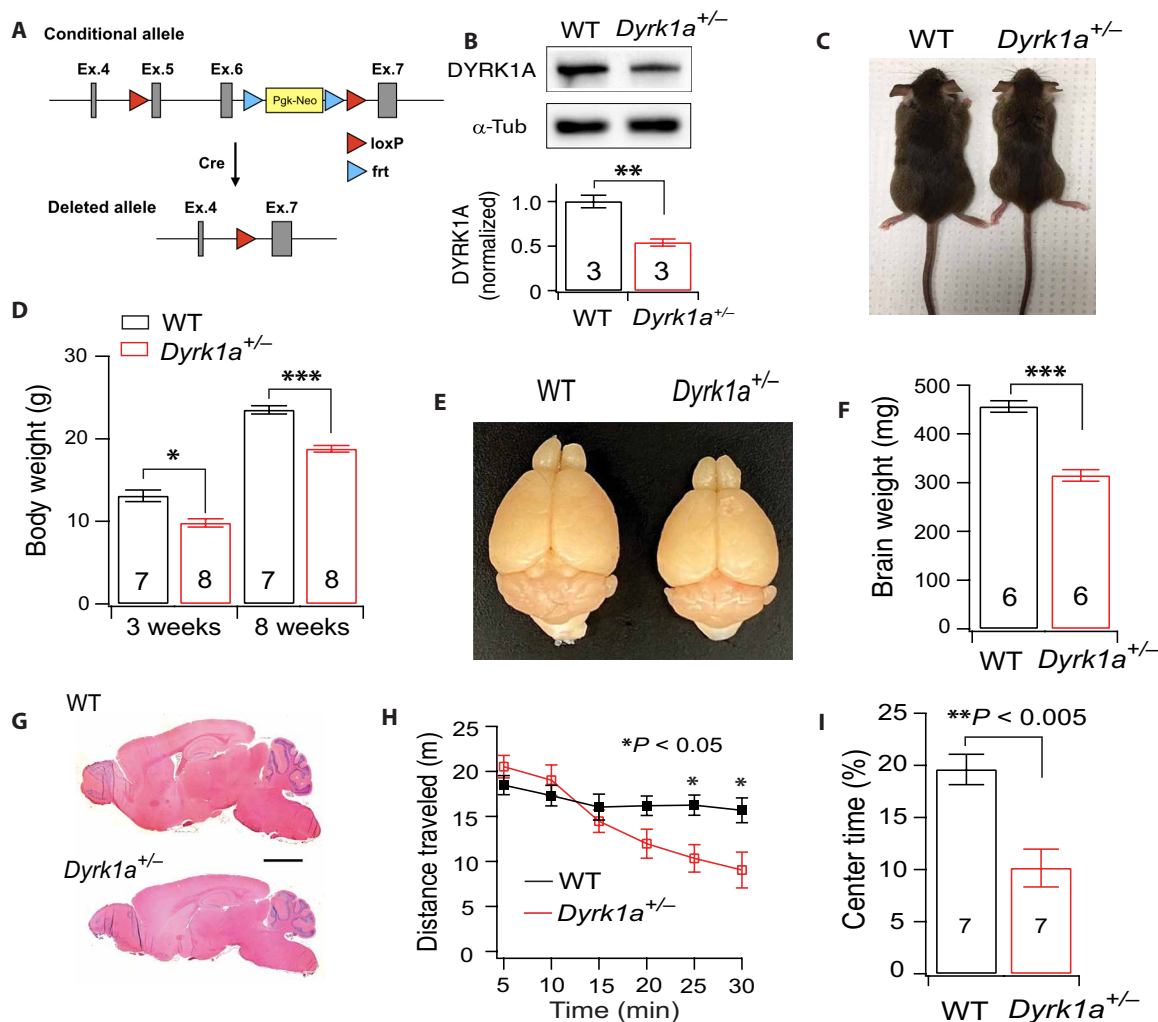
Fig. 10. Heterozygous deletion of *Dyrk1* in mice confirms strain-dependent sensitivity observed in vitro. (**A**) Generation of the null allele of *Dyrk1a* using a conditional *Dyrk1a* allele and constitutively expressed *Cre*. Exons 5 and 6 of Dyrk1a, which encode part of the kinase domain, are flanked by loxP sites. The germline CMV Cre driver removes exons 5 and 6 and the Pgk-Neo selection cassette and causes a frameshift. (**B** to **I**) Phenotype of *Dyrk1a* heterozygotes in B6/129 background. (B) Western blot of cortical tissues from WT and Dyrk1a^{+/−} mice. α-Tub, α-tubulin. (C) A Dyrk1a^{+/−} mouse and a WT littermate at 12 weeks of age. (D) Body weight of male mutant and control mice at 3 and 12 weeks of age. (E) Brains of a control and mutant at 12 weeks of age. (F) Brain weights of mutant and control mice at 12 weeks of age. (G) Sagittal brain sections from a WT and *Dyrk1a^{+/−}* mouse at 3 months of age. Scale bar, 2 mm. (H) Distance traveled by *Dyrk1a^{+/−}* ($n = 7$) and WT ($n = 7$) mice per 5 min in an open field apparatus. (I) Percentage of time spent at the center of the arena. *$P < 0.05$, **$P < 0.01$, and ***$P < 0.001$.

The studies described here address two key questions in precision disease modeling. The first has to do with bridging the gap between in vitro studies and disease models in whole organisms and asks whether disease modeling in genetically diverse mESC tell us what mouse strains are most representative of human phenotypes and thus guide the choice of strain for whole organism studies. More broadly, our study supports the general principle that stem cell–based platform can yield reliable information about the sensitivity or resilience of a particular individual genotype to pathogenic mutations. The second question we addressed asks whether comparisons of in vitro phenotypes from stem cell models in sensitive and resilient mouse strains can yield reliable information about molecular pathways that might be critical to the response to disease mutations in vivo. Our study provides strong validation that cell culture models are predictive of loci of vulnerability to disease variants at the molecular level.

Although human cell culture models provide powerful tools for the genetic analysis of disease, the key phenotypes of interest in many neurodevelopmental disorders (cognition, activity, complex behaviors, and seizures, for example) require study in whole organism models. For most neurodevelopmental conditions, background genetic diversity leads to major phenotypic variation, even for highly penetrant disease variants. Most disease modeling in mice has failed to capture such diversity. The use of large panels of genetically diverse mice addresses this limitation, but the approach is laborious and time consuming. Here, we demonstrate that the parallel use of human and mouse cell culture models has the potential for rapid identification of mouse strains showing patterns of response to pathogenic mutations that are similar to those seen in the same human cell type at the same developmental stage under the same environmental conditions. Thus, at most stages of neurodevelopment,

from embryonic stem cell renewal to neural specification, neurogenesis, and neural maturation and repair, B6-derived cultures were responsive to DYRK1A inhibition or loss, whereas most other strains proved less sensitive. In particular, the proliferative capacity of NPC derived from B6 mice deficient in *Dyrk1a* was reduced relative to controls, whereas other strains were unresponsive to this hallmark effect of *Dyrk1a* loss. We corroborated the effects of chemical DYRK1A inhibition by conducting knockout experiments. Although *DYRK1A* is subject to strong constraint in the human, and most heterozygotes show impairment of neural development, the severity of clinical phenotypes in individuals hemizygous for loss of the gene varies quite considerably (*25*, *62*). In our study, the inhibition of NPC proliferation associated with *Dyrk1a* loss or inhibition seen in B6 reflected the human *DYRK1A* knockout phenotype. It is notable that C57BL/6J hybrid mice or conditional knockouts have been used successfully in a number of studies to model the effects of *DYRK1A* haploinsufficiency in human (*61*, *63*–*66*).

Further in vitro analysis of mESC derived from recombinant inbred strains representing sensitive and resistant genetic backgrounds (B6 and 129, respectively) could identify key modifier genes and potentially target pathways for therapeutic intervention during the early life of affected individuals. A recent elegant study examined the impact of genetic background on phenotype in mice bearing mutations in the *Chd8* autism gene using more than 1000 mice from 33 strains (*13*). Our in vitro model provides a rapid means for probing the cellular and molecular basis of such individual strain differences and for validating the findings in human cells.

This platform will also find application in the study of the basis of genetic variation of repair in the CNS. This is a topic of great interest in traumatic brain injury and stroke, and human culture models will be a powerful adjunct to genetic studies of large patient populations. There were large differences in the axonal regrowth of neurons derived from mESC of different strains in this assay. The robust regrowth of neurons derived from the CAST strain contrasts notably with the poor regrowth of neurons derived from B6 mESC. Our observation of poor axonal regrowth in primary cultures of P5 cortical neurons from B6 compared to WSB mice confirmed the results obtained on neurons derived from mESC. In a number of studies in vivo, B6 mice have been shown to display deficient axonal regeneration relative to 129 or CAST (*67*–*72*), deficiencies that have been attributed either to variation in the inherent capacity for axonal repair or differences in the extent and nature of inflammatory responses in the various strains. Again, strain differences observed in a simple in vitro assay appear to be predictive of whole organism outcomes. Comparative study of neuronal repair in cultures derived from genetically diverse hPSC with the mouse could uncover important pathways for future investigation.

We showed that comparative transcriptomic analysis provided important insight into the molecular pathways and gene networks responsible for sensitivity and resilience to pathogenic mutations. In terms of the effect of Dyrk1a loss on NPC, our study identified the LIF pathway [which regulates neural progenitors in mouse and outer radial glial proliferation in human (*45*)], gene networks related to the transcription factor *Foxb1*, a gene critical in the regulation of neural progenitor proliferation, and two HOX genes involved in hindbrain development (the observation that *Dyrk1a*$^{-/+}$ mice had smaller midbrain and hindbrain in our in vivo study correlates with aspects of our findings in vitro, in which we found that B6-derived NPCs treated with ID-8 had a decreased expression of *Hoxa4* and

Hoxd3). Analysis of the expression of splice isoforms highlight alterations in splicing as an important determinant of susceptibility to *Dyrk1a* haploinsufficiency. The shift in isoform usage of the BDNF receptor *Ntrk2* to a form encoding a protein lacking the kinase domain in the presence of ID-8 in B6 neural progenitors could explain the down-regulation of the BDNF pathway activity observed in a proteomics and phosphoproteomics study of conditional knockout of *Dyrk1a* in the cortical neurons of C57BL/6J mice (*51*). Confirmation of the role of these genes and networks in determining sensitivity of human neural progenitors and their progeny to *DYRK1* haploinsufficiency could identify targets for postnatal therapeutic intervention. For example, antisense oligonucleotides could target alternative splicing at the *NTRK2* locus to restore BDNF response.

Our studies of axonal repair identified the *Ascl1* regulon as a major differential response to injury in both strains either with or without DYRK1A inhibition. In a model of peripheral neuron (dorsal root ganglion) repair, Lisi *et al.* (*59*) noted a differential up-regulation of *Ascl1* in CAST (identified by these authors and by our study as a good regenerator compared to B6) relative to B6. In summary, our in vitro studies comparing gene expression in strains sensitive and resistant to DYRK1A inhibition corroborate in vivo data on key molecular pathways involved in neuronal development and repair and their perturbations in *Dyrk1a*-deficient animals.

The approach we describe here could be generalized to address a range of issues in modeling the genetics of disease. We used a chemical inhibitor and conventional gene knockouts in this study, but screening approaches using short hairpin–mediated RNA interference or single-guide RNA (sgRNA) CRISPR methodologies including Perturb-Seq (*73*) are clearly applicable in this system and could accelerate genetic analysis across large panels of genetically diverse cell lines. We readily applied HCS and medium throughput microelectrode array methodologies in our work. The small panel of mESC used in this study incorporates wide genetic diversity, but we are also developing mESC or iPSC panels from diversity outbred mice and from recombinant inbred strains. These mESC genetic diversity panels have been used for identification of quantitative trait loci and could be used for rapid mapping of modifiers that influence phenotypes of genetic variants implicated in neurodevelopmental disorders. Identification of modifier genes could yield leads for drug discovery and early intervention in patients. We focused here on neural development, but this same approach could be applied to any lineage or tissue that can be generated from PSCs. Facile comparison between phenotypes of human and mouse PSC models in vitro will aid in the identification of those mouse genotypes that confer sensitivity or resilience to disease variants, providing for more precise disease modeling in vivo and reducing the experimental use of animals.

Last, most disease modeling studies using hPSC have been retrospective, replicating the known effects of disease mutations to varying degrees in a culture dish. The use of hPSC and mESC in parallel followed by in vivo studies in the mouse provides a means for prospective testing of the ability of in vitro screens to predict the effects of genetic variants in vivo. This will be an important adjunct to hPSC studies aimed at validating candidate disease variants emerging from genetic studies in humans. Such a strategy will add considerable power to functional genomics analysis of variants of unknown significance or variants for which the role in pathogenesis of disease is undefined. For such variants, establishing a link between observations in cell culture models and precision modeling in vivo will be essential.

Limitations and future directions

We acknowledge that we did not investigate the gender effect in our study, and all stem cells are male-derived. Although autism spectrum disorder (ASD) has a higher rate of affected males, and *DYRK1A* mutation is one of the causes of ASD (*74*), *DYRK1A* haploinsufficiency syndrome does not seem to have a gender bias (*75*). Evaluations of sex-dependent effects can be performed using female-derived stem cells, which are available from our laboratory. In addition, we found that although our protocol can efficiently differentiate genetically diverse stem cells to mature neurons, electrical maturation is achieved at different time rates as proven by our MEA recordings. Recently, Hergenreder *et al.* (*76*) reported that a small-molecule cocktail can accelerate neuronal maturation. Addition of these molecules might synchronize the maturation rate of NPCs from genetically diverse stem cells.

MATERIALS AND METHODS
Resource availability
Materials availability
Dyrk1a$^{-/-}$ mESC strains are available from our laboratory.
Data and code availability
Bulk RNA-seq data have been deposited at GEO and are publicly available as of the date of publication. Accession numbers are listed in the key resources table. This paper does not report original code. Any additional information required to reanalyze the data reported here is available from M.F.P. upon request.
Experimental model and subject details
Note that if not stated otherwise, concentration of reagents are as first described in this paper.

Animals
Experiments were conducted in accordance with the guidelines of the Institutional.

Animal Care and Use Committee of the Jackson Laboratory. For axonal injury/recovery experiments in postnatal neurons, postnatal mice (P3 to P5) from C57BL/6J and WSB/EiJ strains were euthanized by decapitation and cells prepared according to the method below (Preparation of P5 NPC for axonal damage experiments).

Cell lines
mESC from the CC founders (*77*) were used; however, PWD/PhJ was substituted for PWK/PhJ. All mESCs were kept and used under 10 passages to avoid chromosomal rearrangements. All mESCs are male, germ competent, negative for mycoplasma, and retain a normal karyotype. mESC media comprised knockout Dulbecco's modified Eagle's medium (DMEM, no. 10829018, Gibco), 15% fetal calf serum [(FCS embryonic stem)–qualified, no. 10439024, Gibco], 2 mM GlutaMAX (no. 35050061, Gibco), nonessential amino acids (no. 11140050 Gibco), penicillin (50 U/ml), streptomycin (50 µg/ml, no. 15140163, Gibco), 55 µM beta-mercaptoethanol (no. 21985023, Sigma-Aldrich), and 1000 IU of LIF (no. ESG1107 Millipore). Cells were grown on gamma-irradiated mouse embryonic fibroblast feeder cells at 37°C and 5% CO_2. mESCs were passed using trypsin 0.25% (no. 25200056, Gibco).

The KOLF2.1J hiPSC line was used for neural differentiation studies comparing WT and heterozygous knockout cells. CRISPR-Cas9 was used to produce frameshift mutants in Exon 2 on one allele of the *DYRK1A* gene, generating Dyrk1a$^{+/-}$ mutants, as previously described (*78*). Cells were maintained on vitronectin-coated dishes (no. CLS3535-1EA Corning) in mTSR$^+$ media (STEMCELL Technologies) and passed using ReLSR (STEMCELL Technologies).

A panel of 10 genetically diverse hiPSC from the iPSCORE collection (UCSD08i-1-14, UCSD152i-11-3, UCSD140i-37-1, UCSD003i-16-2, UCSD121i-39-2, UCSD094i-25-1, UCSD040i-33-1, UCSD201i-4-2, UCSD123i-74-1, and UCSD134i-80-1) was obtained from WiCell. These cell lines were maintained and passaged as described for KOLF2.1J.

hPSCs were kept and used under 10 passages to avoid chromosomal rearrangements. hPSCs used in this study were karyotyped for chromosomal abnormalities and mycoplasma tested.

Method details
Cortical neuron differentiation of mESC
mESC were cultured as described above. Upon reaching 80% confluency (day 0), cells were trypsinized and seeded on a culture dish for an hour to let feeders attach to the dish. Unattached mESC were recovered and counted. Embriod Body (EB) were formed by seeding 3E5 cells on a well of a six-well plate (ultralow attachment) in mESC media (described above in the "Cell lines" section) plus 10 µM SB431542 and 1 µM dorsomorphin. The next day (day 1), the EB-containing medium was transferred to adherent culture; in a well of a six-well plate previously coated with poly-lysine (PLL; 100 µg/ml, no. P8920, Sigma-Aldrich) for 2 hours and then treated with laminin (Lm; 1 µg/ml, no. L2020 Sigma-Aldrich) and fibronectin (Fn; 5 µg/ml, no. FC010 Millipore) for at least two more hours. After 24 hours (day 2) of seeding the EB in adherent culture, medium was removed and switched to NMM (*27*) (Neurobasal and DMEM/F12, 1:1 v/v) plus SB431542, dorsomorphin, 2 µM I-BET151 (no. 73712, STEMCELL Technologies), and 5 µM retinoic acid (no. R2625, Sigma-Aldrich). Twenty-four hours later (day 3), the medium was removed, and fresh NMM plus SB431542 and dorsomorphin were added. The next day (day 4), SB431542 and dorsomorphin were withdrawn for B6 and WSB, while the other strains were maintained on SB431542 and dorsomorphin for two more days (until day 6), after which the inhibitors were withdrawn. Thereafter, all cells were kept on basal media (NMM) with daily media changes until day 8, when cells were passed to the NPC expansion stage (days 8 to 11). Dissociation of cells into small clumps was done using Tryple Express (no. 12605010, Gibco) and expanded at a 1:2 split ratio on PLL/Fn/Lm–coated dishes in NMM plus FGF2 (20 ng/ml), EGF (20 ng/ml), and RevitaCell (no. A2644501, Gibco). After 24 hours (day 9), Revitacell was removed, but mitogens were daily added for two more days. At day 11, cells were dissociated with Tryple Express to yield a pure population of NPC. NPCs were frozen using Knockout Serum Replacement (no. S2640, Sigma-Aldrich) and 10% dimethyl sulfoxide (no. D2650, Sigma-Aldrich) or passed onto a newly coated plate for neuronal maturation using adult NMM media (formulated with Neurobasal A in place of Neurobasal medium) plus Revitacell, glial cell line–derived neurotrophic factor (GDNF; 10 ng/ml; no. 450-44, PeproTech), BDNF (10 ng/ml; no. 450-02, PeproTech), and 10 µM forskolin (no. 6652995, PeproTech). Next day (day 12), Revitacell was removed. Three days later (day 15), forskolin was removed, and 5 µM 5-fluorodeoxyuridine (no. F0503, Sigma-Aldrich) was added for

1 week (until day 22). After that, adult-NMM supplemented with GDNF and BDNF was changed twice per week.

GABAergic differentiation of mESC

The first 4 days of differentiation were carried out as described in the cortical differentiation protocol above. On day 5, SB431542 and dorsomorphin were removed, and fresh medium was added. On day 6, a sonic hedgehog agonist (SAG; 10 µM; no. 11914, Cayman Chemical Company) was added with every media change and withdrawn after 3 days of neuronal differentiation. The rest of the protocol was exactly the same as the cortical differentiation.

Dopaminergic differentiation of mESC

This procedure was the same as described for GABAergic neurons until day 6. On this day, SAG and FGF8 (100 ng/ml; no. PHG0184 Invitrogen) were added for 2 days, at which point conversion to NPC had occurred. Cells were passed as previously described, with the addition of Revitacell, FGF2, nonessential amino acids, FGF8, SAG, IWP2 (1 µM, no. 681671, Millipore), and LY364947 (3 µM, no. L6293 Sigma-Aldrich) during the expansion stage. After plating cells for maturation, Revitacell, 10 µM forskolin, BDNF, GDNF, ascorbic acid (50 µg/ml, A0278, Sigma-Aldrich), CHIR99021 (3 µM, no. 361571-5MG, Millipore), and LY364947 were added. Medium was changed on the third day with the continued addition of BDNF and GDNF. The cortical neural protocol was followed after day 4 of neuronal differentiation.

Motor neuron differentiation of mESC

Differentiation was as described for cortical neurons until day 7 but with some minor differences. On day 4, SAG and retinoic acid were added to the media cocktail and withdrawn at day 10. On day 7, postmitotic neurons emerged, and cells were ready to be passed and seeded as young MNs. When passing the cells at day 7, medium was swiched from regular NMM to A-NMM. Additives added at day 7 included Revitacell, forskolin, BDNF, GDNF, SAG, and retinoic acid (RA). After 3 days, all additives were withdrawn, but BDNF and GDNF were retained. After this point, half of the media volume was changed two to three times per week.

Cerebral organoid differentiation of mESC

The protocol for organoid formation was based on the cortical differentiation protocol above. Briefly, 2000 cells were seeded per well of a round bottom, ultralow attachment, 96-well plate in mESC basal media with LIF, SB431542, and dorsomorphin. Forty-eight hours later, the spent medium was removed and replaced with NMM+ SB431542, dorsomorphin, I-BET151, and retinoic acid. The next day, this medium was removed, and NMM with SB431542 and Dorsomorphin was added. Forty-eight hours later, half the volume of the culture medium was replaced. At days 6 and 8, half of the medium was replaced with basal media (NMM). On day 10, the organoids were split evenly and 24 organoids were placed into 6-cm ultralow attachment dishes. On day 16, organoids were embedded in undiluted Matrigel (Corning, 356234, lot 229001) in the same medium and kept on a shaker at 16 rpm for at least 21 days.

hPSC-derived NPC

The protocol was the same as the one used for mESC with a few modifications. IBet151 and RA were added at day 1 instead of day 2 (still 24-hour treatment). Instead of mESC media, mTSR+ medium was used. SB431542 and dorsomorphin were added until day 11. From days 11 to 14, the cells were kept in basal NMM media. At day 14, the differentiated NPCs were passed and expanded using bFGF and EGF for 3 days. Afterward, the cells were frozen or used for further experiments.

hPSC Neurosphere assay

Human NPCs were seeded on a 96-well ultralow attachment plate at various concentrations (2000, 8000, 16,000, and 32000 cells) for 15 passages in NMM + FGF2 and EGF. Media changes were performed every other day. Spheroids were imaged with a Leica Dmi1 microscope, and their size was calculated using ImageJ software. Spheroids were passed every 4 days using Accutase (STEMCELL Technologies 07920) for 30 min at 37°C.

EdU labeling of NPC

Cells were incubated for 2 hours with 5 µM 5-Ethynyl-2'-deoxyUridine (EdU). After 48 hours, cells were harvested and fixed with 4% paraformaldehyde at room temperature for 15 min. EdU incorporation was detected according to the Clik-iT EdU Alexa Fluor 594 flow cytometry assay kit protocol (no. C10339, Thermo Fisher Scientific). Cells not labeled with EdU were used as negative control.

hiPSC-derived cortical neurons

The protocol was similar as the one used for mESC but with slight modifications. Cells were dissociated with Accutase. 5E5 cells were seeded on a well of a low-attachment six-well plate in the presence of SB431542, dorsomorphin, Ibet151, RA, and Y-27632. Twenty-four hours later in mTSR+ medium, EB were sedimented under unit gravity, the medium was removed, and 4 ml of mTeSR+ media supplemented with SB434512 and dorsomorphin was added. EB were seeded in a PLL/Fn/Lm–coated well of the same size and incubated for 24 hours, after which the medium was replaced with NMM + SB434512 and dorsomorphin. This medium was changed every day until day 11, at which point small molecules were withdrawn, and incubation with basal media continued for 3 more days. Cells were dissociated into clumps of cells and re-seeded at a 1:2 split ratio on PLL/Fn/Lm–coated dishes in the presence of bFGF and EGF for 2 or 3 days for NPC expansion, with the addition of Rock inhibitor on the first day. NPC could be frozen as with the mESC, or cells were plated for neuronal differentiation, but 5-FluoroDeoxyUridine5FDU (5FDU) is added at day 7 for 7 days.

Differentiation of hPSC into motor neurons

Cell were differentiated according to the hPSC to cortical neuron protocol with minor modifications. On day 8, retinoic acid and SAG were added, and cells were maintained in this medium until day 23. Every time cells were passed, fibronectin and laminin (5 µg/ml each) were supplemented in the media in addition to their usage in the plate coating; these were supplemented again twice per week to avoid cell detachment and until 10 days after withdrawal of mitogens.

Differentiation of hPSC into cerebral organoids

Initial differentiation was similar to 2D cortical cultures but adapted for organoids by culturing in suspension, embedding in Matrigel, and growing under agitation. Four thousand iPSCs were seeded in 100 µl of media per well of a 96-well plate with all aforementioned molecules. The following day, cultures were switched to mTeSR plus with SB434512 and dorsomorphin. Next day, this medium was replaced with IDM [DMEM-F12 GlutaMAX and Neurobasal 1:1 (v/v) ratio, N2 supplement, insulin (5 µg/ml), nonessential amino acids, penicillin-streptomycin, and B27 supplement without Vit A (no. 12587010, Gibco)] with SB431542 and dorsomorphin. This medium was changed every other day until day 11. At this point, the organoids were embedded in Matrigel. The cultures were incubated in 6 ml of media overnight and, on the following day, transferred to an orbital shaker with an orbit of 1.9 cm (0.75 inch) at 69 rpm. On day 18, half

the media volume was replaced with fresh media. On day 20, Matrigel was removed and the medium switched to NMM. From then on, the medium was changed two to three times a week. On day 30, cultures were switched to A-NMM adult with media changes two to three times per week.

Differentiation of hPSC into dopaminergic organoids
Adaptation of the cortical organoid differentiation protocol was done as follows. SAG was added from day 4 until day 11 when it was withdrawn. FGF8 was added from day 6 until day 11 when it was withdrawn. LY36947 and IWP2 were added at day 8 until days 11 and 15, respectively. CHIR99021 and ascorbic acid were added on day 11 until days 15 and 30, respectively.

Calcium spike assay
Organoids were assayed using the FLIPR Calcium 6 Assay Kit (Molecular Devices). Briefly, organoids were incubated for 2 hours in half FLIPR Calcium 6 reconstituted reagent and half NMM media. Afterward, this medium was removed and fresh medium was added. Organoids were immediately transferred to Opera plus microscope (PerkinElmer) under controlled environmental conditions (37C and 5% CO_2 in a humidified chamber). Images were taken every 0.7 s up to 400 frames. Calcium spikes were analyzed using the integrated Harmony software by recognizing individual cells and tracking fluorophore intensity over time.

Electrophysiological recordings
NPCs were seeded on a previously coated MEA plate and left to mature as described above. However, for the MEA plates, a 10-μl droplet containing 50,000 mouse NPCs or 20,000 human NPCs was seeded at the center of each well of a 48-well plate (CitoView MEA 48, Axion Biosystems). After the cells attached (≈7 hours), more medium was added to properly cover the well. Recordings were obtained on days 7, 14, 21, 28, 35, and 42. Spontaneous activity was recorded on an Axion Maestro Pro at 37°C for 10 min using the AxiS navigator software. Recordings were analyzed using the built-in spike detector at 6× STD.

Axonal damage using mESC-derived neurons
NPC of each cell line were seeded on one of the two chambers of a microfluidic device (eNUVIO). Devices were precoated with PLL/Fn/Lm. Cells were left to mature for 4 days. Afterward, in the contralateral chamber, axons were cut off by scratching the chamber and pipetting the media up and down several times. The axonal chamber was rinsed to remove debris and replenished with fresh media and Fn/Lm to enhance axonal attachment. Four days later, the axonal side was treated with Calcein AM (C1430, Thermo Fisher Scientific), and images of the entire device were taken. The area covered by axons was analyzed using ImageJ.

Preparation of p5 NPC for axonal damage experiments
C57BL/6J (B6) and WSB/EiJ (WSB) P5 animals were euthanized as described above. The hippocampus/dentate gyrus was dissected, mechanically dissociated, and seeded on PLL/Fn/Lm–coated dishes in NMM media plus EGF and FGF (20 μg/ml each) and expanded through one passage. At this point, expanded NPCs were used for axonal damage experiments in the same fashion as mESC-derived NPCs described above.

Immunostaining
Cultures were washed with phosphate-buffered saline (PBS) and fixed with 4% paraformaldehyde 4% for 15 min and finally washed again with PBS three more times. Blocking and permeabilization were carried out using 5% bovine serum albumin and 0.3% Triton X-100 for an hour at room temperature. Primary antibodies used were OTX2 (1:1000, Millipore, AB9566-1), TUBB3 (1:1000; BioLegend, 801202), Ki67 (1:50; Santa Cruz Biotechnology, SC-23900), PAX6 (1:1000; BioLegend, 862001), Brachyury (1:200; R&D Systems, AF2085), Vglut (1:200; Abcam, ab104898), CHAT (1:200; Merck Millipore, AB144P), Hb9 (1:200; Thermo Fisher Scientific, PA5-67195), MCM2 (1:500; Abcam, ab95361), DYRK1A (1:1000; Cell Signaling Technology), ISL1 (both undiluted 1:1; DSHB, 40.3A4-S and 40.2D6-S), SOX2 (1:500; Millipore, AB5603), Eomes (1:1000; Abcam, ab23345), POU5F1 (1:500; BD, 611202), GATA4 (1:2000; Santa Cruz Biotechnology, SC-25310), NANOG (1:500; PeproTech, 500-P236-50UG), SOX1 (1:500; R&D Systems, AF3369-SP), AFP (1:500; Dako, A0008), glial fibrillary acidic protein (1:1000; Dako, Z0334), NeuroD1 (1:2000; Abcam, ab60704), TH (1:1000; Pel-Freez, P41301), GAD 65/67 (1:250; Millipore, ABN904), vgat (1:200; Synaptic Systems, 131011), and Reelin (1:200; Abcam, ab78540). Primary antibodies were incubated overnight and washed three times with PBS, and secondary ALEXA antibodies (1:1000) against primary antibodies were incubated for 2 hours. 4′,6-diamidino-2-phenylindole was used for nuclear counterstaining. Cerebral organoids were cleared and stained using fructose-glycerol clearing method (79), and antibodies were used at twice the concentrations described above.

High content microscopy
PerkinElmer cell carrier ultra 96-well plates were used for high-content microscopy. Imaging was carried out on the Operetta CSL (PerkinElmer) microscope, and image analysis was done using Harmony software.

Reverse transcription PCR
Samples were collected, and RNA was prepared using QIAGEN RNAeasy plus mini kit (QIAGEN). Reverse transcription was carried out using the High-Capacity RNA-to-cDNA Kit (Thermo Fisher Scientific). Real-time PCR was conducted using QuantStudio 7 Flex on a two-step cycle run using TaqMan Probes (Oct4, no. 4331182; Nanog, no. 4331182; Otx2, no. 4331182; Pax6, no. 4331182; Tubb3, no. 4351372; Scl17a7, no. 4331182; Gapdh, no. 4453320).

Bulk RNA-seq
Samples were collected, and RNA was prepared using QIAGEN RNA column system. mRNA libraries were made at 150 ×2 with at least 30 million reads per sample.

Transcriptomic analysis
Low-quality bases ($Q < 30$) from the 3′ end of reads were removed, and reads with more than 30% low-quality bases ($Q < 30$) overall were filtered out. Trimmed reads were aligned to the reference genome using bowtie2 (80), generating a bam file that was used by RSEM for quantification providing expression counts for genes and isoforms separately. Quality metrics were obtained at the fastq and bam level. This includes metrics such as total number of reads, total number of high-quality reads, and alignment rate. The RNA-seq data were filtered and normalized. MDS plots were made using EdgeR (81). Venn diagrams were made using systemPipeR (82), and the Limma (83) package was used for barcode plots and testing for multiple gene sets. GO analysis and plotting were completed using TopGO (84) and GO.db (85). Transcriptional network analysis was done using RTN (86). Circos plots were made using circlize (87). Isoform switching was analyzed using IsoformSwitchAnalyzeR package (88) and other tools to import data, conduct normalization, isoform switch testing, prediction of open reading frames, premature termination decay, coding, domaings signal peptides, protein disorder, and consequences (88–94).

Statistical analysis

Statistical details can be found within the figure legends. Computation and plots were done using Rstudio and GraphPad Prism.

SNP and transcript variant analysis

Dyrk1a sequences were pulled from the mouse genome project (https://mousegenomes.org/) and compared for number of SNPs and transcript variants per strains. Sequence variants were aligned using Clustal O multiple sequence alignment. Sequences downloaded from http://informatics.jax.org/mgv/.

QTL analysis

Diversity outbred mESC eQTL and protein QTL analysis are previously published (15, 37) and available at https://churchilllab.jax.org/qtlviewer/ DO_mESC and https://doi.org/10.6084/m9.figshare.22012850. Data for Dyrk1a were accessed through publicly available data sources. QTL mapping was performed using a linear-mixed model implemented in the "scan1" function in R/qtl2 package with rank normal scores, sex of the cell lines as an additive covariate, and the leave one chromosome out option for kinship correction (citations for R/qtl2 and DOQTL).

Western blot

Cells were lysed with NP40 cell lysis buffer supplemented with protease inhibitor cocktail (P2714, Sigma-Aldrich). Cells were centrifuged for 15 min at 12,000g at 4°C. Supernatant was saved and kept frozen until further use. DC protein assay (Bio-Rad) was used to quantify protein. The cell lysate was placed in SDS sample buffer and run in a precasted gel at 100 V. Proteins were transferred into nitrocellulose using the trans-Blot turbo (Bio-Rad). Primary antibodies are described above. Secondary antibodies were goat anti-Rb horseradish peroxidase (1:10,000; Abcam, ab6721) and horse anti-mouse (VectorLabs, PI-2000-1). Detection was performed using SuperSignal Atto (Thermo Fisher Scientific) using a G box documentation system (Syngene).

Generation of Dyrk1a null allele

Mice carrying Dyrk1a null allele were generated by mating male mice homozygous of conditional Dyrk1a floxed allele (JAX strain, no. 027801) with female mice hemizygous of the germline CMV-Cre (JAX strain, no. 006054). Both strains were on a B6 background. Genotyping was performed by PCR on tail DNA. The PCR primers for Dyrk1a alleles are as follows: forward 5′-CCTGGA GAAGAGGGCAAG-3′ (common), reverse 5′-GGCATAACTTGCATACAGTGG-3′ (WT and floxed allele), and reverse 5′-ACT GTG TGA GGA GTC TTG ACA-3′ (null allele), which give products of 132, 232, and 295 base pairs (bp) for WT, floxed, and null allele, respectively. The PCR primers for CMV-Cre are as follows: forward 5′-GCATTACCGGTCGAT GCAACGAGTGATGAG-3′ and reverse 5′-GAGTGAACGAAC CTGGTCGAAATCAGTGCG-3′, which gives a product of 410 bp for the transgene.

The cross between floxed Dyrk1a and CMV-Cre on B6 background did not produce any pups heterozygous of Dyrk1a null allele (0 of 93 pups), but a few live pups were mosaic for floxed and null allele. Crossing male mosaic mice to WT B6 females did not produce any pups (0 of 46 pups). In contrast, crossing the same male mosaic mice to WT 129S1 females produced live pups heterozygous of Dyrk1a null allele ($Dyrk1a^{+/-}$, 15 of 81 pups). Further backcrossing to 129S1 produced $Dyrk1a^{+/-}$ mice at Mendelian ratios.

Phenotyping of Dyrk1a$^{+/-}$ mice

Mice on 129B6 F1 background were used for phenotyping. Western blots were performed with cortical tissues obtained from $Dyrk1a^{+/-}$ and WT mice at 13 weeks of age, using standard procedures and antibodies against DYRK1A (1:1000; Cell Signaling Technology, no. 8756) and α-tubulin (1:5000, loading control; Thermo Fisher Scientific, no. A11126). Protein levels were quantified using ImageJ. For each sample, DYRK1A protein level was normalized to that of α-tubulin.

Activity of mice was analyzed at 10 to 12 weeks of age with an open field apparatus where a single mouse was allowed to explore freely for 30 min and recorded by video. Activity was analyzed using idTracker (95). Distance traveled per 5 min and time spent in the center square were quantified.

For brain weight and morphology, mice were euthanized at 12 weeks of age and perfused with 4% paraformaldehyde. Whole brains were dissected and weighted. Brain sections were cut at 70-μm thickness and stained with hematoxylin and eosin method.

Dyrk1a knockout mESC

C57Bl6/J mESC (line no. 49) were grown on irradiated mouse embryo fibroblasts in 2i/FCS/LIF media (14). Exon 3 of Dyrk1a (Dyrk1a-202, ENMUST00000119878) was deleted in ESC using CRISPR-Cas9. Briefly, oligos encoding guide RNAs targeting intron 2 and intron 3 of murine Dyrk1a were cloned into plasmid pX459 v2.0 (Addgene, plasmid no. 62988) and sequence-verified. Plasmids encoding Dyrk1a sgRNAs were transfected into mouse ESC using Lipofectamine 3000 (Thermo Fisher Scientific, L30000001) at a ratio of 1-μg total plasmid per 200,000 cells. After 24 hours, cells were transferred to irradiated DR4 puromycin-resistant mouse embryo fibroblasts, and transfected cells were selected for 40 hours with puromycin (1 μg/ml). Cells were then removed from puromycin selection and cultured for 1 week, and then individual colonies were picked into 96-well plates. Clones were genotyped by PCR with primers Dyrk1a_For (5′-CATTCCATGCTGCTGGCCTTC-3′) and Dyrk1a_ Rev: 5′-GCCAGCAGCATGGAATGAGAAC-3′) and analyzed by gel electrophoresis. Clones completely missing a WT band (1712 bp) were further expanded and regenotyped for confirmation of loss of exon 3.

Supplementary Materials

This PDF file includes:
Figs. S1 to S7
Table S1
Legend for movie S1

Other Supplementary Material for this manuscript includes the following:
Movie S1

REFERENCES AND NOTES

1. S. Ghosh, R. Nehme, L. E. Barrett, Greater genetic diversity is needed in human pluripotent stem cell models. *Nat. Commun.* **13**, 7301 (2022).

2. C. H. Chandler, S. Chari, I. Dworkin, Does your gene need a background check? How genetic background impacts the analysis of mutations, genes, and evolution. *Trends Genet.* **29**, 358–366 (2013).

3. R. P. Erickson, Mouse models of human genetic disease: Which mouse is more like a man? *Bioessays* **18**, 993–998 (1996).

4. J. D. Riordan, J. H. Nadeau, From peas to disease: Modifier genes, network resilience, and the genetics of health. *Am. J. Hum. Genet.* **101**, 177–191 (2017).

5. M. P. Keller, D. M. Gatti, K. L. Schueler, M. E. Rabaglia, D. S. Stapleton, P. Simecek, M. Vincent, S. Allen, A. T. Broman, R. Bacher, C. Kendziorski, K. W. Broman, B. S. Yandell, G. A. Churchill, A. D. Attie, Genetic drivers of pancreatic islet function. *Genetics* **209**, 335–356 (2018).

6. R. T. Molenhuis, H. Bruining, M. J. V. Brandt, P. E. van Soldt, H. J. Abu-Toamih Atamni, J. P. H. Burbach, F. A. Iraqi, R. F. Mott, M. J. H. Kas, Modeling the quantitative nature of neurodevelopmental disorders using collaborative cross mice. *Mol. Autism* **9**, 63 (2018).

7. S. M. Neuner, S. E. Heuer, M. J. Huentelman, K. M. S. O'Connell, C. C. Kaczorowski, Harnessing genetic complexity to enhance translatability of alzheimer's disease mouse models: A path toward precision medicine. *Neuron* **101**, 399–411.e5 (2019).

8. H. Li, J. Auwerx, Mouse systems genetics as a prelude to precision medicine. *Trends Genet.* **36**, 259–272 (2020).

9. S. J. Moore, G. G. Murphy, V. A. Cazares, Turning strains into strengths for understanding psychiatric disorders. *Mol. Psychiatry* **25**, 3164–3177 (2020).

10. K. D. Onos, A. Uyar, K. J. Keezer, H. M. Jackson, C. Preuss, C. J. Acklin, R. O'Rourke, R. Buchanan, T. L. Cossette, S. J. Sukoff Rizzo, I. Soto, G. W. Carter, G. R. Howell, Enhancing face validity of mouse models of Alzheimer's disease with natural genetic variation. *PLOS Genet.* **15**, e1008155 (2019).

11. L. J. Sittig, P. Carbonetto, K. A. Engel, K. S. Krauss, C. M. Barrios-Camacho, A. A. Palmer, Genetic background limits generalizability of genotype-phenotype relationships. *Neuron* **91**, 1253–1259 (2016).

12. E. Swanzey, C. O'Connor, L. G. Reinholdt, Mouse genetic reference populations: Cellular platforms for integrative systems genetics. *Trends Genet.* **37**, 251–265 (2021).

13. M. Tabbaa, A. Knoll, P. Levitt, Mouse population genetics phenocopies heterogeneity of human Chd8 haploinsufficiency. *Neuron* **111**, 539–556.e5 (2023).

14. A. Czechanski, C. Byers, I. Greenstein, N. Schrode, L. R. Donahue, A. K. Hadjantonakis, L. G. Reinholdt, Derivation and characterization of mouse embryonic stem cells from permissive and nonpermissive strains. *Nat. Protoc.* **9**, 559–574 (2014).

15. D. A. Skelly, A. Czechanski, C. Byers, S. Aydin, C. Spruce, C. Olivier, K. Choi, D. M. Gatti, N. Raghupathy, G. R. Keele, A. Stanton, M. Vincent, S. Dion, I. Greenstein, M. Pankratz, D. K. Porter, W. Martin, C. O'Connor, W. Qin, A. H. Harrill, T. Choi, G. A. Churchill, S. C. Munger, C. L. Baker, L. G. Reinholdt, Mapping the effects of genetic variation on chromatin state and gene expression reveals loci that control ground state pluripotency. *Cell Stem Cell* **27**, 459–469.e8 (2020).

16. T. A. Garbutt, T. I. Konneker, K. Konganti, A. E. Hillhouse, F. Swift-Haire, A. Jones, D. Phelps, D. L. Aylor, D. W. Threadgill, Permissiveness to form pluripotent stem cells may be an evolutionarily derived characteristic in Mus musculus. *Sci. Rep.* **8**, 14706 (2018).

17. E. Swanzey, T. F. McNamara, E. Apostolou, M. Tahiliani, M. Stadtfeld, A susceptibility locus on chromosome 13 profoundly impacts the stability of genomic imprinting in mouse pluripotent stem cells. *Cell Rep.* **30**, 3597–3604.e3 (2020).

18. D. Ortmann, S. Brown, A. Czechanski, S. Aydin, D. Muraro, Y. Huang, R. A. Tomaz, A. Osnato, G. Canu, B. T. Wesley, D. A. Skelly, O. Stegle, T. Choi, G. A. Churchill, C. L. Baker, P. J. Rugg-Gunn, S. C. Munger, L. G. Reinholdt, L. Vallier, Naive pluripotent stem cells exhibit phenotypic variability that is driven by genetic variation. *Cell Stem Cell* **27**, 470–481.e6 (2020).

19. M. B. Fernando, T. Ahfeldt, K. J. Brennand, Modeling the complex genetic architectures of brain disease. *Nat. Genet.* **52**, 363–369 (2020).

20. F. Tejedor, X. R. Zhu, E. Kaltenbach, A. Ackermann, A. Baumann, I. Canal, M. Heisenberg, K. F. Fischbach, O. Pongs, Minibrain: A new protein kinase family involved in postembryonic neurogenesis in Drosophila. *Neuron* **14**, 287–301 (1995).

21. C. Branca, D. M. Shaw, R. Belfiore, V. Gokhale, A. Y. Shaw, C. Foley, B. Smith, C. Hulme, T. Dunckley, B. Meechoovet, A. Caccamo, S. Oddo, Dyrk1 inhibition improves Alzheimer's disease-like pathology. *Aging Cell* **16**, 1146–1154 (2017).

22. A. Feki, Y. Hibaoui, DYRK1A protein, a promising therapeutic target to improve cognitive deficits in Down syndrome. *Brain Sci.* **8**, 187 (2018).

23. P. Fernández-Martínez, C. Zahonero, P. Sánchez-Gómez, DYRK1A: The double-edged kinase as a protagonist in cell growth and tumorigenesis. *Mol. Cell. Oncol.* **2**, e970048 (2015).

24. T. Dang, W. Y. Duan, B. Yu, D. L. Tong, C. Cheng, Y. F. Zhang, W. Wu, K. Ye, W. X. Zhang, M. Wu, B. B. Wu, Y. An, Z. L. Qiu, B. L. Wu, Autism-associated Dyrk1a truncation mutants impair neuronal dendritic and spine growth and interfere with postnatal cortical development. *Mol. Psychiatry* **23**, 747–758 (2018).

25. R. K. Earl, T. N. Turner, H. C. Mefford, C. M. Hudac, J. Gerdts, E. E. Eichler, R. A. Bernier, Clinical phenotype of ASD-associated DYRK1A haploinsufficiency. *Mol. Autism.* **8**, 54 (2017).

26. M. L. Arbones, A. Thomazeau, A. Nakano-Kobayashi, M. Hagiwara, J. M. Delabar, DYRK1A and cognition: A lifelong relationship. *Pharmacol. Ther.* **194**, 199–221 (2019).

27. N. Gaspard, T. Bouschet, A. Herpoel, G. Naeije, J. van den Ameele, P. Vanderhaeghen, Generation of cortical neurons from mouse embryonic stem cells. *Nat. Protoc.* **4**, 1454–1463 (2009).

28. M. Bibel, J. Richter, K. Schrenk, K. L. Tucker, V. Staiger, M. Korte, M. Goetz, Y.-A. Barde, Differentiation of mouse embryonic stem cells into a defined neuronal lineage. *Nat. Neurosci.* **7**, 1003–1009 (2004).

29. J. Bian, J. Zheng, S. Li, L. Luo, F. Ding, Sequential differentiation of embryonic stem cells into neural epithelial-like stem cells and oligodendrocyte progenitor cells. *PLOS ONE* **11**, e0155227 (2016).

30. S. M. Pollard, R. Wallbank, S. Tomlinson, L. Grotewold, A. Smith, Fibroblast growth factor induces a neural stem cell phenotype in foetal forebrain progenitors and during embryonic stem cell differentiation. *Mol. Cell. Neurosci.* **38**, 393–403 (2008).

31. Q.-L. Ying, A. G. Smith, Defined conditions for neural commitment and differentiation. *Methods Enzymol.* **365**, 327–341 (2003).

32. Y. Shi, P. Kirwan, F. J. Livesey, Directed differentiation of human pluripotent stem cells to cerebral cortex neurons and neural networks. *Nat. Protoc.* **7**, 1836–1846 (2012).

33. T. Miyabayashi, M. Yamamoto, A. Sato, S. Sakano, Y. Takahashi, Indole derivatives sustain embryonic stem cell self-renewal in long-term culture. *Biosci. Biotechnol. Biochem.* **72**, 1242–1248 (2008).

34. K. Hasegawa, S. Y. Yasuda, J. L. Teo, C. Nguyen, M. McMillan, C. L. Hsieh, H. Suemori, N. Nakatsuji, M. Yamamoto, T. Miyabayashi, C. Lutzko, M. F. Pera, M. Kahn, Wnt signaling orchestration with a small molecule DYRK inhibitor provides long-term xeno-free human pluripotent cell expansion. *Stem Cells Transl. Med.* **1**, 18–28 (2012).

35. M. B. Monteiro, S. Ramm, V. Chandrasekaran, S. A. Boswell, E. J. Weber, K. A. Lidberg, E. J. Kelly, V. S. Vaidya, A high-throughput screen identifies DYRK1A inhibitor ID-8 that stimulates human kidney tubular epithelial cell proliferation. *J. Am. Soc. Nephrol.* **29**, 2820–2833 (2018).

36. S. F. Bellmaine, D. A. Ovchinnikov, D. T. Manallack, C. E. Cuddy, A. G. Elefanty, E. G. Stanley, E. J. Wolvetang, S. J. Williams, M. Pera, Inhibition of DYRK1A disrupts neural lineage specification in human pluripotent stem cells. *eLife* **6**, e24502 (2017).

37. S. Aydin, D. T. Pham, T. Zhang, G. R. Keele, D. A. Skelly, J. A. Paulo, M. Pankratz, T. Choi, S. P. Gygi, L. G. Reinholdt, C. L. Baker, G. A. Churchill, S. C. Munger, Genetic dissection of the pluripotent proteome through multi-omics data integration. *Cell Genom.* **3**, 100283 (2023).

38. Q. L. Ying, J. Wray, J. Nichols, L. Batlle-Morera, B. Doble, J. Woodgett, P. Cohen, A. Smith, The ground state of embryonic stem cell self-renewal. *Nature* **453**, 519–523 (2008).

39. J. Nichols, J. Silva, M. Roode, A. Smith, Suppression of Erk signalling promotes ground state pluripotency in the mouse embryo. *Development* **136**, 3215–3222 (2009).

40. C. B. Pantazis, A. Yang, E. Lara, J. A. M. Donough, C. Blauwendraat, L. Peng, H. Oguro, J. Kanaujiya, J. Zou, D. Sebesta, G. Pratt, E. Cross, J. Blockwick, P. Buxton, L. Kinner-Bibeau, C. Medura, C. Tompkins, S. Hughes, M. Santiana, F. Faghri, M. A. Nalls, D. Vitale, S. Ballard, Y. A. Qi, D. M. Ramos, K. M. Anderson, J. Stadler, P. Narayan, J. Papademetriou, L. Reilly, M. P. Nelson, S. Aggarwal, L. U. Rosen, P. Kirwan, V. Pisupati, S. L. Coon, S. W. Scholz, T. Priebe, M. Öttl, J. Dong, M. Meijer, L. J. M. Janssen, V. S. Lourenco, R. van der Kant, D. Crusius, D. Paquet, A.-C. Raulin, G. Bu, A. Held, B. J. Wainger, R. M. C. Gabriele, J. M. Casey, S. Wray, D. Abu-Bonsrah, C. L. Parish, M. S. Beccari, D. W. Cleveland, E. Li, I. V. L. Rose, M. Kampmann, C. C. Aristoy, P. Verstreken, L. Heinrich, M. Y. Chen, B. Schüle, D. Dou, E. L. F. Holzbaur, M. C. Zanellati, R. Basundra, M. Deshmukh, S. Cohen, R. Khanna, M. Raman, Z. S. Nevin, M. Matia, J. Van Lent, V. Timmerman, B. R. Conklin, K. J. Chase, K. Zhang, S. Funes, D. A. Bosco, L. Erlebach, M. Welzer, D. Kronenberg-Versteeg, G. Lyu, E. Arenas, E. Coccia, L. Sarrafha, T. Ahfeldt, J. C. Marioni, W. C. Skarnes, M. R. Cookson, M. E. Ward, F. T. Merkle, A reference human induced pluripotent stem cell line for large-scale collaborative studies. *Cell Stem Cell* **29**, 1685–1702.e22 (2022).

41. Y. Zhang, E. Hoxha, T. Zhao, X. Zhou, G. Alvarez-Bolado, Foxb1 regulates negatively the proliferation of oligodendrocyte progenitors. *Front. Neuroanat.* **11**, 53 (2017).

42. J. van de Leemput, N. C. Boles, T. R. Kiehl, B. Corneo, P. Lederman, V. Menon, C. Lee, R. A. Martinez, B. P. Levi, C. L. Thompson, S. Yao, A. Kaykas, S. Temple, C. A. Fasano, CORTECON: A temporal transcriptome analysis of in vitro human cerebral cortex development from human embryonic stem cells. *Neuron* **83**, 51–68 (2014).

43. T. Alexander, C. Nolte, R. Krumlauf, Hox genes and segmentation of the hindbrain and axial skeleton. *Annu. Rev. Cell Dev. Biol.* **25**, 431–456 (2009).

44. T. Shimazaki, T. Shingo, S. Weiss, The ciliary neurotrophic factor/leukemia inhibitory factor/gp130 receptor complex operates in the maintenance of mammalian forebrain neural stem cells. *J. Neurosci.* **21**, 7642–7653 (2001).

45. M. G. Andrews, C. Siebert, L. Wang, M. L. White, J. Ross, R. Morales, M. Donnay, G. Bamfonga, T. Mukhtar, A. A. McKinney, K. Gemenes, S. Wang, Q. Bi, E. E. Crouch, N. Parikshak, G. Panagiotakos, E. Huang, A. Bhaduri, A. R. Kriegstein, LIF signaling regulates outer radial glial to interneuron fate during human cortical development. *Cell Stem Cell* **30**, 1382–1391.e5 (2023).

46. S. Desai, M. Ding, B. Wang, Z. Lu, Q. Zhao, K. Shaw, W. K. Yung, J. N. Weinstein, M. Tan, J. Yao, Tissue-specific isoform switch and DNA hypomethylation of the pyruvate kinase PKM gene in human cancers. *Oncotarget* **5**, 8202–8210 (2014).

47. D. Toiber, G. Azkona, S. Ben-Ari, N. Toran, H. Soreq, M. Dierssen, Engineering DYRK1A overdosage yields Down syndrome-characteristic cortical splicing aberrations. *Neurobiol. Dis.* **40**, 348–359 (2010).

48. J. Shi, T. Zhang, C. Zhou, M. O. Chohan, X. Gu, J. Wegiel, J. Zhou, Y. W. Hwang, K. Iqbal, I. Grundke-Iqbal, C. X. Gong, F. Liu, Increased dosage of Dyrk1A alters alternative splicing factor (ASF)-regulated alternative splicing of tau in Down syndrome. *J. Biol. Chem.* **283**, 28660–28669 (2008).

49. M. Alvarez, X. Estivill, S. de la Luna, DYRK1A accumulates in splicing speckles through a novel targeting signal and induces speckle disassembly. *J. Cell Sci.* **116**, 3099–3107 (2003).

50. S. Ding, J. Shi, W. Qian, K. Iqbal, I. Grundke-Iqbal, C. X. Gong, F. Liu, Regulation of alternative splicing of tau exon 10 by 9G8 and Dyrk1A. *Neurobiol. Aging* **33**, 1389–1399 (2012).

51. J. A. Levy, C. W. LaFlamme, G. Tsaprailis, G. Crynen, D. T. Page, Dyrk1a mutations cause undergrowth of cortical pyramidal neurons via dysregulated growth factor signaling. *Biol. Psychiatry* **90**, 295–306 (2021).

52. H. Togashi, T. Sakisaka, Y. Takai, Cell adhesion molecules in the central nervous system. *Cell Adh. Migr.* **3**, 29–35 (2009).

53. A. Majer, S. J. Medina, D. Sorensen, M. J. Martin, K. L. Frost, C. Phillipson, K. Manguiat, S. A. Booth, The cell type resolved mouse transcriptome in neuron-enriched brain tissues from the hippocampus and cerebellum during prion disease. *Sci. Rep.* **9**, 1099 (2019).

54. S. Ning, J. S. Pagano, G. N. Barber, IRF7: Activation, regulation, modification and function. *Genes Immun.* **12**, 399–414 (2011).

55. P. H. Ozdinler, R. S. Erzurumlu, Slit2, a branching-arborization factor for sensory axons in the Mammalian CNS. *J. Neurosci.* **22**, 4540–4549 (2002).

56. K. M. Ori-McKenney, R. J. McKenney, H. H. Huang, T. Li, S. Meltzer, L. Y. Jan, R. D. Vale, A. P. Wiita, Y. N. Jan, Phosphorylation of β-tubulin by the down syndrome kinase, minibrain/dyrk1a, regulates microtubule dynamics and dendrite morphogenesis. *Neuron* **90**, 551–563 (2016).

57. M. Martinez de Lagran, R. Benavides-Piccione, I. Ballesteros-Yanez, M. Calvo, M. Morales, C. Fillat, J. Defelipe, G. J. Ramakers, M. Dierssen, Dyrk1A influences neuronal morphogenesis through regulation of cytoskeletal dynamics in mammalian cortical neurons. *Cereb. Cortex* **22**, 2867–2877 (2012).

58. D. Cortes, M. F. Pera, The genetic basis of inter-individual variation in recovery from traumatic brain injury. *NPJ Regen Med* **6**, 5 (2021).

59. V. Lisi, B. Singh, M. Giroux, E. Guzman, M. W. Painter, Y. C. Cheng, E. Huebner, G. Coppola, M. Costigan, C. J. Woolf, K. S. Kosik, Enhanced neuronal regeneration in the CAST/Ei mouse strain is linked to expression of differentiation markers after injury. *Cell Rep.* **20**, 1136–1147 (2017).

60. M. Quiles Del Rey, J. D. Mancias, NCOA4-mediated ferritinophagy: A potential link to neurodegeneration. *Front. Neurosci.* **13**, 238 (2019).

61. V. Fotaki, M. Dierssen, S. Alcántara, S. Martinez, E. Martí, C. Casas, J. Visa, E. Soriano, X. Estivill, M. L. Arbonés, Dyrk1A haploinsufficiency affects viability and causes developmental delay and abnormal brain morphology in mice. *Mol. Cell. Biol.* **22**, 6636–6647 (2002).

62. C. R. Murray, S. N. Abel, M. B. McClure, J. Foster II, M. I. Walke, P. Jayakar, G. Bademci, M. Tekin, Novel causative variants in DYRK1A, KARS, and KAT6A associated with intellectual disability and additional phenotypic features. *J Pediatr Genet* **6**, 77–83 (2017).

63. S. R. Ferron, N. Pozo, A. Laguna, S. Aranda, E. Porlan, M. Moreno, C. Fillat, S. de la Luna, P. Sánchez, M. L. Arbonés, I. Fariñas, Regulated segregation of kinase Dyrk1A during asymmetric neural stem cell division is critical for EGFR-mediated biased signaling. *Cell Stem Cell* **7**, 367–379 (2010).

64. R. Benavides-Piccione, M. Dierssen, I. Ballesteros-Yanez, M. Martinez de Lagran, M. L. Arbones, V. Fotaki, J. DeFelipe, G. N. Elston, Alterations in the phenotype of neocortical pyramidal cells in the Dyrk1A+/− mouse. *Neurobiol. Dis.* **20**, 115–122 (2005).

65. G. Arqué, V. Fotaki, D. Fernández, M. M. de Lagrán, M. L. Arbonés, M. Dierssen, Impaired spatial learning strategies and novel object recognition in mice haploinsufficient for the dual specificity tyrosine-regulated kinase-1 (Dyrk1A). *PLOS ONE* **3**, e2575 (2008).

66. M. Raveau, A. Shimohata, K. Amano, H. Miyamoto, K. Yamakawa, DYRK1A-haploinsufficiency in mice causes autistic-like features and febrile seizures. *Neurobiol. Dis.* **110**, 180–191 (2018).

67. T. Omura, K. Omura, A. Tedeschi, P. Riva, M. W. Painter, L. Rojas, J. Martin, V. Lisi, E. A. Huebner, A. Latremoliere, Y. Yin, L. B. Barrett, B. Singh, S. Lee, T. Crisman, F. Gao, S. Li, K. Kapur, D. H. Geschwind, K. S. Kosik, G. Coppola, Z. He, S. T. Carmichael, L. I. Benowitz, M. Costigan, C. J. Woolf, Robust axonal regeneration occurs in the injured CAST/Ei mouse CNS. *Neuron* **86**, 1215–1227 (2015).

68. L. Dimou, L. Schnell, L. Montani, C. Duncan, M. Simonen, R. Schneider, T. Liebscher, M. Gullo, M. E. Schwab, Nogo-A-deficient mice reveal strain-dependent differences in axonal regeneration. *J. Neurosci.* **26**, 5591–5603 (2006).

69. A. Tedeschi, T. Omura, M. Costigan, CNS repair and axon regeneration: Using genetic variation to determine mechanisms. *Exp. Neurol.* **287**, 409–422 (2017).

70. D. M. Basso, L. C. Fisher, A. J. Anderson, L. B. Jakeman, D. M. McTigue, P. G. Popovich, Basso mouse scale for locomotion detects differences in recovery after spinal cord injury in five common mouse strains. *J. Neurotrauma* **23**, 635–659 (2006).

71. M. Ma, P. Wei, T. Wei, R. M. Ransohoff, L. B. Jakeman, Enhanced axonal growth into a spinal cord contusion injury site in a strain of mouse (129X1/SvJ) with a diminished inflammatory response. *J. Comp. Neurol.* **474**, 469–486 (2004).

72. K. A. Kigerl, V. M. McGaughy, P. G. Popovich, Comparative analysis of lesion development and intraspinal inflammation in four strains of mice following spinal contusion injury. *J. Comp. Neurol.* **494**, 578–594 (2006).

73. J. M. Replogle, R. A. Saunders, A. N. Pogson, J. A. Hussmann, A. Lenail, A. Guna, L. Mascibroda, E. J. Wagner, K. Adelman, G. Lithwick-Yanai, N. Iremadze, F. Oberstrass, D. Lipson, J. L. Bonnar, M. Jost, T. M. Norman, J. S. Weissman, Mapping information-rich genotype-phenotype landscapes with genome-scale Perturb-seq. *Cell* **185**, 2559–2575.e28 (2022).

74. A. K. Halladay, S. Bishop, J. N. Constantino, A. M. Daniels, K. Koenig, K. Palmer, D. Messinger, K. Pelphrey, S. J. Sanders, A. T. Singer, J. L. Taylor, P. Szatmari, Sex and gender differences in autism spectrum disorder: Summarizing evidence gaps and identifying emerging areas of priority. *Mol. Autism.* **6**, 36 (2015).

75. L. E. Meissner, E. F. Macnamara, P. D'Souza, J. Yang, G. Vezina, N. Undiagnosed Diseases, C. R. Ferreira, W. M. Zein, C. J. Tifft, D. R. Adams, DYRK1A pathogenic variants in two patients with syndromic intellectual disability and a review of the literature. *Mol. Genet. Genomic Med.* **8**, e1544 (2020).

76. E. Hergenreder, Y. Zorina, Z. Zhao, H. Munguba, E. L. Calder, A. Baggiolini, A. P. Minotti, R. M. Walsh, C. Liston, J. Levitz, R. Garippa, S. Chen, G. Ciceri, L. Studer, Combined small molecule treatment accelerates timing of maturation in human pluripotent stem cell-derived neurons (2022); https://doi.org/10.1101/2022.06.02.494616.

77. E. J. Chesler, D. R. Miller, L. R. Branstetter, L. D. Galloway, B. L. Jackson, V. M. Philip, B. H. Voy, C. T. Culiat, D. W. Threadgill, R. W. Williams, G. A. Churchill, D. K. Johnson, K. F. Manly, The collaborative cross at oak ridge national laboratory: Developing a powerful resource for systems genetics. *Mamm. Genome* **19**, 382–389 (2008).

78. A. Andersson-Rolf, R. C. Mustata, A. Merenda, J. Kim, S. Perera, T. Grego, K. Andrews, K. Tremble, J. C. Silva, J. Fink, W. C. Skarnes, B. K. Koo, One-step generation of conditional and reversible gene knockouts. *Nat. Methods* **14**, 287–289 (2017).

79. J. F. Dekkers, M. Alieva, L. M. Wellens, H. C. R. Ariese, P. R. Jamieson, A. M. Vonk, G. D. Amatngalim, H. Hu, K. C. Oost, H. J. G. Snippert, J. M. Beekman, E. J. Wehrens, J. E. Visvader, H. Clevers, A. C. Rios, High-resolution 3D imaging of fixed and cleared organoids. *Nat. Protoc.* **14**, 1756–1771 (2019).

80. Z. Wei, W. Zhang, H. Fang, Y. Li, X. Wang, esATAC: An easy-to-use systematic pipeline for ATAC-seq data analysis. *Bioinformatics* **34**, 2664–2665 (2018).

81. M. D. Robinson, D. J. McCarthy, G. K. Smyth, edgeR: A Bioconductor package for differential expression analysis of digital gene expression data. *Bioinformatics* **26**, 139–140 (2010).

82. T. W. H. Backman, T. Girke, systemPipeR: NGS workflow and report generation environment. *BMC Bioinformatics* **17**, 388 (2016).

83. M. E. Ritchie, B. Phipson, D. Wu, Y. Hu, C. W. Law, W. Shi, G. K. Smyth, limma powers differential expression analyses for RNA-sequencing and microarray studies. *Nucleic Acids Res.* **43**, e47 (2015).

84. A. Alexa, J. Rahnenfuhrer, topGO: Enrichment Analysis for Gene Ontology (2023). doi:10.18129/B9.bioc.topGO, R package version 2.54.0; https://bioconductor.org/ packages/topGO.

85. M. Carlson, GO.db: A set of annotation maps describing the entire Gene Ontology (2019). R package version 3.8.2.

86. M. N. Fletcher, M. A. Castro, X. Wang, I. de Santiago, M. O'Reilly, S. F. Chin, O. M. Rueda, C. Caldas, B. A. Ponder, F. Markowetz, K. B. Meyer, Master regulators of FGFR2 signalling and breast cancer risk. *Nat. Commun.* **4**, 2464 (2013).

87. Z. Gu, L. Gu, R. Eils, M. Schlesner, B. Brors, Circlize implements and enhances circular visualization in R. *Bioinformatics* **30**, 2811–2812 (2014).

88. K. Vitting-Seerup, B. T. Porse, A. Sandelin, J. Waage, spliceR: An R package for classification of alternative splicing and prediction of coding potential from RNA-seq data. *BMC Bioinformatics* **15**, 81 (2014).

89. J. J. Almagro Armenteros, K. D. Tsirigos, C. K. Sonderby, T. N. Petersen, O. Winther, S. Brunak, G. von Heijne, H. Nielsen, SignalP 5.0 improves signal peptide predictions using deep neural networks. *Nat. Biotechnol.* **37**, 420–423 (2019).

90. R. D. Finn, J. Mistry, J. Tate, P. Coggill, A. Heger, J. E. Pollington, O. L. Gavin, P. Gunasekaran, G. Ceric, K. Forslund, L. Holm, E. L. Sonnhammer, S. R. Eddy, A. Bateman, The Pfam protein families database. *Nucleic Acids Res.* **38**, D211–D222 (2010).

91. W. Huber, V. J. Carey, R. Gentleman, S. Anders, M. Carlson, B. S. Carvalho, H. C. Bravo, S. Davis, L. Gatto, T. Girke, R. Gottardo, F. Hahne, K. D. Hansen, R. A. Irizarry, M. Lawrence, M. I. Love, J. MacDonald, V. Obenchain, A. K. Oles, H. Pages, A. Reyes, P. Shannon, G. K. Smyth, D. Tenenbaum, L. Waldron, M. Morgan, Orchestrating high-throughput genomic analysis with bioconductor. *Nat. Methods* **12**, 115–121 (2015).

92. B. Mészáros, G. Erdos, Z. Dosztányi, IUPred2A: Context-dependent prediction of protein disorder as a function of redox state and protein binding. *Nucleic Acids Res.* **46**, W329–W337 (2018).

93. K. Vitting-Seerup, A. Sandelin, IsoformSwitchAnalyzeR: Analysis of changes in genome-wide patterns of alternative splicing and its functional consequences. *Bioinformatics* **35**, 4469–4471 (2019).

94. L. Wang, H. J. Park, S. Dasari, S. Wang, J. P. Kocher, W. Li, CPAT: Coding-potential assessment tool using an alignment-free logistic regression model. *Nucleic Acids Res.* **41**, e74 (2013).

95. A. Pérez-Escudero, J. Vicente-Page, R. C. Hinz, S. Arganda, G. G. de Polavieja, idTracker: Tracking individuals in a group by automatic identification of unmarked animals. *Nat. Methods* **11**, 743–748 (2014).